Asymmetric Electron Acceptors for High-Efficiency and Low-Energy-Loss Organic Photovoltaics

Shuixing Li, Lingling Zhan, Yingzhi Jin, Guanqing Zhou, Tsz-Ki Lau, Ran Qin, Minmin Shi, Chang-Zhi Li, Haiming Zhu, Xinhui Lu, Fengling Zhang and Hongzheng Chen

Li, S., Zhan, L., Jin, Y., Zhou, G., Lau, T., Qin, R., Shi, M., Li, C., Zhu, H., Lu, X., Zhang, F., Chen, H., (2020), Asymmetric Electron Acceptors for High-Efficiency and Low-Energy-Loss Organic Photovoltaics, *Advanced Materials*, , 2001160. https://doi.org/10.1002/adma.202001160

Original publication available at:
https://doi.org/10.1002/adma.202001160

DOI: 10.1002/((please add manuscript number))
Article type: Communication

Asymmetric Electron Acceptors for High-Efficiency and Low-Energy-Loss Organic Photovoltaics

Shuixing Li, Lingling Zhan, Yingzhi Jin, Guanqing Zhou, Tsz-Ki Lau, Ran Qin, Minmin Shi, Chang-Zhi Li, Haiming Zhu, Xinhui Lu, Fengling Zhang,* and Hongzheng Chen**

Dr. S. Li, Dr. L. Zhan, R. Qin, Prof. M. Shi, Prof. C.-Z. Li, Prof. H. Chen
State Key Laboratory of Silicon Materials, MOE Key Laboratory of Macromolecular Synthesis and Functionalization, Department of Polymer Science and Engineering, Zhejiang University, 310027 Hangzhou, P. R. China
E-mail: minminshi@zju.edu.cn, hzchen@zju.edu.cn
Y. Jin, Prof. F. Zhang
Department of Physics, Chemistry and Biology (IFM), Linköping University, 581 83 Linköping, Sweden.
E-mail: fengling.zhang@liu.se
Prof. H. Zhu
Department of Chemistry, Zhejiang University, 310027 Hangzhou, P. R. China.
Dr. T.-K. Lau, Prof. X. Lu
Department of Physics, Chinese University of Hong Kong, New Territories, 999077 Hong Kong, P. R. China.
G. Zhou
School of Chemistry and Chemical Engineering, and Center for Advanced Electronic Materials and Devices, Shanghai Jiao Tong University, 200240 Shanghai, P. R. China.

Keywords: asymmetric acceptor, high-efficiency, low-energy-loss, organic photovoltaics, charge separation

Low energy loss and efficient charge separation under small driving forces are the prerequisites for realizing high power conversion efficiency (PCE) in organic photovoltaics (OPVs). Here, a new molecular design of non-fullerene acceptors (NFAs) is proposed to address above two issues simultaneously by introducing asymmetric terminals. Two NFAs, BTP-S1 and BTP-S2, are constructed by introducing halogenated indandione (A_1) and 3-dicyanomethylene-1-indanone (A_2) as two different conjugated terminals on the central fused core (D), wherein they share the same backbone as well-known NFA Y6, but at different terminals. Such asymmetric NFAs with A_1-D-A_2 structure exhibit superior photovoltaic properties when blended with polymer donor PM6. Energy loss analysis reveals that asymmetric molecule BTP-S2 with six chlorine atoms attached at terminals enables the

corresponding devices to give an outstanding electroluminescence quantum efficiency of 2.3 $\times 10^{-2}$ %, one order of magnitude higher than the devices based on symmetric Y6 (4.4×10^{-3} %), thus significantly lowering the non-radiative loss and energy loss of the corresponding devices. Besides, asymmetric BTP-S1 and BTP-S2 with multiple halogen atoms at terminals exhibit fast hole transfer to donor PM6. As a result, OPVs based on PM6:BTP-S2 blend realize a PCE of 16.37%, higher than that (15.79%) of PM6:Y6-based cells. A further optimization of ternary blend (PM6:Y6:BTP-S2) results in a best PCE of 17.43%, which is among the highest efficiencies for single-junction OPVs. This work provides an effective approach to simultaneously lower the energy loss and promote the charge separation of OPVs by molecular design strategy.

Organic photovoltaics (OPVs) with bulk-heterojunction (BHJ) active layers have recently received a big progress in efficiencies, which is mainly benefitted from the material innovations in p-type donors and n-type acceptors.[1-5] Especially for non-fullerene acceptors (NFAs) with acceptor-donor-acceptor (A-D-A) structure, the evolution of electron-rich core (D), such as indacenodithienothiophene (IDTT), dithieno[2",3":4',5']thieno[2',3':4,5]pyrrolo[3,2-e:2',3'-g][2,1,3]benzothiadiazole (BTP), cyclopentadithiophene, and phenyl-thiophene, and electron-deficient terminals (A), such as halogenation and conjugation extension, has created a number of high-performance materials with tunable absorptions from visible to near-infrared (NIR) ranges and energy levels.[6-12] BTP-based NFAs originated by Zou's group, such as Y6 and its derivatives, possess unique features of dominant face-on orientation, high mobility and low energy loss with high electroluminescence quantum efficiency (EQE_{EL}) in devices, thus enabling OPVs with over 17% efficiencies.[13-19] It is interesting to note that efficient NFAs could exhibit relatively low energy loss and fast charge separation under small driving forces, compared with fullerene-based acceptors.[20-22] Although some progresses have been made, energy loss in OPVs based on NFAs is still obviously large, compared to Si and

perovskite counterparts.[23] A common way to lower the energy loss of OPV is to narrow the energy level offsets between p-type donor and n-type acceptor in BHJ, but this inevitably affects the charge separation efficiency in BHJ.[24] Thus, exploring new strategies for mitigating energy loss of OPVs is of importance through the innovations in molecular structure while without sacrificing the charge separation efficiency.

Among the materials design strategies, halogenation plays an important role in boosting the device performances.[25-28] Halogen atoms, such as fluorine and chlorine atoms, can bring benefits to NFAs, including intermolecular interaction, polarization of molecule, increase of electrostatic potential, and adjustment of energy levels.[29-31] It is also reported that halogenation on NFAs has a positive effect on reducing energy loss of OPVs.[13] Among the three parts of energy loss (radiative loss above bandgap, radiative loss below bandgap, and non-radiative loss), non-radiative loss is the critical factor influencing the energy loss, which can be lowered by enhancing EQE_{EL} of the devices.[32-35] Thus, it is attractive to answer the question that whether halogen type and number at the terminals of NFAs affect the EQE_{EL}, and thus holding back the energy loss.

Based on the above intention, we here propose a new molecular design strategy for NFAs with A_1-D-A_2 asymmetric structure: asymmetric electron acceptors containing indandione and 3-dicyanomethylene-1-indanone as two different terminals. Different from the NFAs with an asymmetric donor core D, such NFAs with asymmetric terminals of A_1 and A_2 can be synthesized in a more feasible method by utilizing the difference in reactivity between indandione and 3-dicyanomethylene-1-indanone, and thus avoiding complicated synthetic processes of the asymmetric core.[36-38] Besides, this strategy also diversifies the types of NFAs through combination of various D, A_1 and A_2 building blocks. Especially, it enables us to introduce six halogen atoms on the terminals, providing a good example for us to study energy loss for NFAs with more halogen atoms. Therefore, two asymmetric NFAs of BTP-S1 and BTP-S2 with a BTP core and various halogen atoms are synthesized as shown in **Figure**

1a. We find that the OPVs based on the blends containing polymer donor PM6 and asymmetric BTP-S2 with six chlorine atoms show the highest EQE_{EL}, thus lowering the non-radiative loss. Meanwhile, faster hole transfer from BTP-S2 to PM6 is also measured in their blends. As a result, the best efficiency of 16.37% is achieved for binary OPVs based on PM6:BTP-S2 blend among the studied structures in this work, and an increased efficiency to 17.43% is further delivered from ternary OPVs based on PM6:Y6:BTP-S2 blend, which is one of the best results among reported single-junction OPVs.

To synthesize asymmetric NFAs, we firstly obtained a 4,5,6,7-tetrachloroindane-1,3-dione (I-4Cl) as one kind of terminal via a reduction reaction. Then using a BTP unit as the molecular donor core, BTP-S1 or BTP-S2 (**Figure 1a**) was synthesized via two steps of Knoevenagel condensation: in the first step, I-4Cl was used as the end-capping group on one side, in the second step, 5,6-difluoro-3-(dicyanomethylene)indanone (IC-2F) or 5,6-dichloro-3-(dicyanomethylene)indanone (IC-2Cl) was used as the end-capping group on the other side. During the synthesis of BTP-S2, the symmetric product with two I-4Cl as the terminals was also obtained as BTP-S3 (**Figure S1,** Supporting Information). Although cyano-group was removed on one side, both BTP-S1 and BTP-S2 showed good thermal stability with decomposition temperatures (T_d, 5% weight loss) of 360 and 330 °C, respectively (**Figure S2,** Supporting Information). The synthetic and characterization details can be found in the Supporting Information.

For asymmetric terminated NFAs (BTP-S1 and BTP-S2), one unique feature is the introduction of up to six halogen atoms at the terminals. Another feature is the removal of cyano-group on one side, which is quite different from the traditional symmetric NFAs like Y6. It is thus essential to examine the effects of such molecular designing on the optical and electrochemical properties, which are guideline for choosing donors to pair with. As shown in **Figure 1c**, both BTP-S1 and BTP-S2 show absorptions close to 880 nm, which are blue-shifted by around 50 nm when compared with Y6's absorptions. The reason for such blue-

shifting is the weakening of quinoid resonance effect that originated from the delocalization of π-electron on cyano-group.[39] BTP-S2 exhibits a bit narrower optical bandgap than BTP-S1, due to the enhanced intramolecular charge transfer effect induced by the two chlorine atoms on IC terminal. Besides, BTP-S2 shows higher absorption coefficient than BTP-S1 (**Figure 1b**). However, both BTP-S1 and BTP-S2 can still maintain NIR absorptions. But, if cyano-group is removed on both sides, the resulting symmetric molecule, BTP-S3, can only show absorption up to around 780 nm (**Figure S3,** Supporting Information). Therefore, asymmetric terminated NFAs combining indandione and 3-dicyanomethylene-1-indanone can realize suitable absorptions to pair with wide bandgap donors for high photocurrents.

To verify the energy levels of NFAs, cyclic voltammetry method was applied (**Figure S4,** Supporting Information). It was found that BTP-S1 and BTP-S2 possessed the same electron affinity (EA) of -4.01 eV, indicating that I-4Cl also has strong electronegativity. As for the ionization potential (IP), BTP-S2 had the same IP of -5.65 eV as Y6, while BTP-S1 owned a higher-lying IP of -5.55 eV. Interestingly, BTP-S1 and BTP-S2 possess similar absorption edges, but there presents a big difference in electrochemical bandgap. To further prove that there indeed exists a large difference in IP values between BTP-S1 and BTP-S2, ultraviolet photoelectron spectroscopy (UPS) was also performed and a large IP difference of 0.15 eV was detected (**Figure S4c,** Supporting Information). Based on the above information, we chose a wide bandgap polymer PM6 (chemical structure shown in **Figure S1,** Supporting Information) as the donor blended with our NFAs to study the photovoltaic performances, since PM6 not only owns complementary absorption to those of NFAs as shown in **Figure 1c**, but also a deep IP value of -5.48 eV for obtaining high voltages as shown in **Figure 1d**.

Geometry of an NFA is the critical factor to affect the blend morphology of active layer in OPVs.[40] We performed a density functional theory calculation at B3LYP/6-31G level to get the optimized configurations of BTP-S1, BTP-S2 and Y6 (**Figure S5,** Supporting Information). For Y6 molecule, there are two features that help form suitable domain sizes:

one is the upright alkyl chains on the pyrrole rings and another is the twisted backbone. Thus, the dihedral angle at the center caused by the twisted backbone may play an important role. Through calculation, we find that, in addition to the alkyl chains nearly vertical to the backbones, the dihedral angles at the centers are 10.93° for BTP-S1, 10.82° for BTP-S2 and 10.72° for Y6. The larger dihedral angle may lead to smaller domain sizes, which is proven in the following morphology characterization.

To evaluate the photovoltaic performances, we utilized a conventional device geometry of indium tin oxide/PEDOT:PSS/Active Layer/PFN-Br/Ag. To obtain the optimal device fabrication conditions, donor/acceptor (D/A) weight ratio, additive volume ratio, and thermal annealing temperature were optimized. The optimization process can be found in **Table S1** and **S2,** Supporting Information. For OPVs based on PM6:BTP-S1 blend, the optimal conditions were a D/A weight ratio of 1:1, the addition of 0.8% (v/v) 1-chloronaphthalene (CN) and thermal annealing at 100 °C for 10 min. The optimal conditions were a D/A weight ratio of 1:1.2, the addition of 0.5% (v/v) CN and thermal annealing at 115 °C for 10 min for OPVs based on PM6:BTP-S2 blend. For PM6:Y6-based OPVs, the optimal conditions (a D/A weight ratio of 1:1.2, the addition of 0.5% CN and thermal annealing at 100 °C for 10 min) were adopted directly from literature.[7] The champion *J-V* curves are displayed in **Figure 2a** and the relevant photovoltaic parameters are summarized in **Table 1**. It is obvious that main differences exist in the open-circuit voltage (V_{oc}) and short-circuit current density (J_{sc}), while all three types of devices show similar fill factors (FFs) of ~72%. Y6-based OPVs had the highest J_{sc} due to the most red-shifted and broadest absorption as well as large absorption coefficient. BTP-S2-based OPVs showed a higher J_{sc} of 24.07 mA cm^{-2} than that of 22.39 mA cm^{-2} in BTP-S1-based OPVs, indicating a more efficient photon to electron conversion in BTP-S2-based OPVs. More interesting phenomenon presented in the V_{oc} variations. Y6-based OPVs showed a V_{oc} of 0.842 V, which was the same as reported result in the literature.[7] BTP-S1-based OPVs delivered a V_{oc} of 0.934 V, corresponding to an increase of 0.092 V

compared with that of Y6-based OPVs. Surprisingly, although BTP-S2 has a slightly narrower bandgap than BTP-S1, BTP-S2-based OPVs exhibited a higher V_{oc} of 0.945 V than that of BTP-S1-based OPVs, which means BTP-S2-based OPVs achieve a larger reduced energy loss than BTP-S1-based OPVs (**Figure 2b**). Such enhancement of V_{oc} for BTP-S1-based and BTP-S2-based OPVs is uncommon and favorable, demonstrating very low energy losses among the best results reported so far (**Figure 2c**). Due to the simultaneous improvements in V_{oc} and J_{sc}, a champion power conversion efficiency (PCE) of 16.37% was realized in BTP-S2-based OPVs with good reproducibility (**Figure 2d**), obviously higher than that of BTP-S1-based OPVs (15.21%) (**Figure S6,** Supporting Information) or Y6-based OPVs (15.79%) (**Figure 2e**). From above results, we can see that asymmetric terminated electron acceptors are capable of obtaining a higher V_{oc}, and also a higher PCE, compared with the symmetric counterparts. Besides, the asymmetric molecule (BTP-S2) with only chlorine atoms attached performs better than the one (BTP-S1) with both fluorine and chlorine atoms attached. However, removing all the cyano-groups on both sides (BTP-S3), the OPVs based on PM6:BTP-S3 blend only showed a PCE of 8.22%, although the V_{oc} was as high as 1.09 V, indicating asymmetric electron acceptors with only cyano-group removed on one side are the optimal choice (**Figure S7,** Supporting Information), suggesting the potential of the asymmetric terminals for high-performance NFA design.

External quantum efficiency (EQE) curves of relevant OPVs are presented in **Figure 2f**. All three types of OPVs could reach over 80% EQE values. BTP-S2-based OPVs showed higher EQE values both in donor and acceptor absorption ranges than BTP-S1-baesd OPVs, partly attributing to the higher absorption coefficients of PM6:BTP-S2 blend than PM6:BTP-S1 blend in both donor and acceptor absorption ranges (**Figure S8,** Supporting Information). Y6-based OPVs exhibited the highest EQE values in the acceptor absorption ranges caused by the highest absorption coefficient of PM6:Y6 blend in the acceptor absorption ranges, indicating cyano-group is beneficial for improving absorption coefficient. The integrated

current densities from the EQE curves were 25.30 mA cm^{-2} for PM6:Y6-based OPVs, 21.73 mA cm^{-2} for PM6:BTP-S1-based OPVs and 23.22 mA cm^{-2} for PM6:BTP-S2-baesd OPVs, which are consistent with the results from *J-V* curves with small errors (less than 4%). The device stability of OPVs was examined under continuous light illumination (**Figure S9,** Supporting Information). It was found that all three types of OPVs showed similar results with over 90% initial PCEs remained after light soaking for 360 min.

As presented above, both BTP-S1 and BTP-S2-based OPVs exhibit high V_{oc} of 0.934 and 0.945 V, respectively, while Y6-based OPVs show a V_{oc} of 0.842 V. Of course, the bandgaps of three types of OPVs are different. Thus, to compare the energy loss, we should perform a detailed calculation. Based on Shockley-Queisser (SQ) limit, the energy loss can be separated into three parts as shown in Equation (1)[41]

$$E_{loss} = E_g - qV_{oc} = \left(E_g - qV_{oc}^{SQ}\right) + \left(qV_{oc}^{SQ} - qV_{oc}^{rad}\right) + \left(qV_{oc}^{rad} - qV_{oc}\right)$$
$$= \left(E_g - qV_{oc}^{SQ}\right) + q\Delta V_{oc}^{rad,below\ gap} + q\Delta V_{oc}^{non-rad} = \Delta E_1 + \Delta E_2 + \Delta E_3 \quad (1)$$

where, ΔE_1 is the radiative loss above bandgap, ΔE_2 is the radiative loss below bandgap, and ΔE_3 is the non-radiative loss. The maximum voltage (V_{oc}^{SQ}) is calculated according to the SQ limit (the EQE is assumed to be 1 above the bandgap and 0 below the bandgap). Radiative loss above bandgap is unavoidable with the value of 0.25~0.30 eV. Radiative loss below bandgap, nowadays, can be smaller than 0.10 eV for NFA-based OPVs. As for the non-radiative loss, it is another main part of energy loss in OPVs. Therefore, reducing non-radiative loss is the main approach for reducing energy loss. The non-radiative loss can also be calculated by measuring the EQE_{EL} of the relevant OPVs through Equation (2):

$$\Delta E_3 = q\Delta V_{oc}^{non-rad} = -kTln(EQE_{EL}) \quad (2)$$

where, k is the Boltzmann constant, T is the temperature, and EQE_{EL} is the electroluminescence quantum efficiency of the OPVs when the injected current is equal to the J_{sc} of the devices under 1 sun illumination.

To calculate detailed energy losses, we should first determine the bandgap E_g. The E_g is determined from the derivatives of the Fourier transform photocurrent spectroscopy (FTPS)-EQE curve (see **Figure 3a** and **Figure S10** and **S11,** Supporting Information) and a mean peak energy is calculated by the Equation (3)[42]

$$E_g = \frac{\int_a^b E_g P(E_g) dE_g}{\int_a^b P(E_g) dE_g} \quad (3)$$

where the integration limits a and b are chosen as the P(a) = P(b) = 0.5Max[P(E_g)]. The bandgaps were calculated as 1.42 eV for PM6:Y6-based device, 1.49 eV for PM6:BTP-S1-based device and 1.48 eV for PM6:BTP-S2-based device. The detailed energy losses are summarized in **Table 2**. For three types of OPVs, energy loss is gradually reduced from 0.58 eV for PM6:Y6-based device to 0.56 eV for PM6:BTP-S1-baesd device and to 0.53 eV for PM6:BTP-S2-based device. The differences in energy losses mainly originated from the changes in non-radiative losses. In **Table 2**, both ΔE_3 and experimental (*Exp.*)$q\Delta V_{oc}^{non-rad}$ represent non-radiative losses, but calculated through different methods. ΔE_3 is calculated through the equation of $\Delta E_3 = qV_{oc}^{rad} - qV_{oc}$, wherein V_{oc} is measured voltage extracted from the *J-V* curves. *Exp.* $q\Delta V_{oc}^{non-rad}$ is calculated with Equation (2) as shown above. *Exp.*$q\Delta V_{oc}^{non-rad}$ can be easily obtained by measuring the EQE_{EL} values of devices. As shown in **Figure 3b**, PM6:Y6-based device showed an EQE_{EL} of 4.4 × 10^{-3} %, PM6:BTP-S1-based device showed an EQE_{EL} of 1.1 × 10^{-2} %, while PM6:BTP-S2-based device showed the highest EQE_{EL} of 2.3 ×10^{-2} %, thus, the non-radiative losses were found to be 0.26 eV for PM6:Y6-based device, 0.24 eV for PM6:BTP-S1-based device, and 0.22 eV for PM6:BTP-S2-based device. Significantly, the EQE_{EL} can realize order of magnitude of improvement, and such a high EQE_{EL} of 2.3 ×10^{-2} % is rarely reported for high-efficiency OPVs. Without doubts, introducing more halogen atoms can indeed reduce non-radiative loss and chlorine atom will be better than fluorine atom. To further check above argument, we also measured

the EQE_{EL} of OPV based on PM6:BTP-S3 blend film (see **Figure S12,** Supporting Information), since BTP-S3 owns eight chlorine atoms at the terminals. It was found that an EQE_{EL} as high as 5.8×10^{-2} % was detected for PM6:BTP-S3-based device, corresponding to the lowest non-radiative loss of 0.19 eV. Above results demonstrate that asymmetric terminated electron acceptors with six halogen atoms are good materials for realizing low energy losses.

It is well known that fast charge separation under small driving force (< 0.3 eV) can be realized for NFA systems.[22,43-45] The driving force can also be simplified as the energy level offsets between the donors and acceptors. Although the above phenomenon is common, there still remain many puzzles to be solved. One key question to be answered is that, between molecular structure (like halogen type or number at the terminals) and the values of energy level offsets, which one would make larger impact on the charge separation, in case positive driving force is maintained. In the three non-fullerene systems of PM6:BTP-S1, PM6:BTP-S2 and PM6:Y6, EA offsets are all maintained over 0.3 eV and IP offsets are all maintained less than 0.2 eV. So, we can try to answer the above question in two cases: electron transfer at over 0.3 eV offset and hole transfer at less than 0.2 eV offset.

We then employed femtosecond (fs) transient absorption (TA) spectra to study the hole transfer and electron transfer processes in the blends of PM6:BTP-S1, PM6:BTP-S2 and PM6:Y6. The results are displayed in **Figure S13-S15,** Supporting Information. Since the main absorption peaks of the donor and acceptors are well separated, we thus can extract both spectral and temporal characteristics of charge transfer dynamics.[46,47] It was found that both PM6:BTP-S1 and PM6:BTP-S2 blends showed a bit faster hole transfer than PM6:Y6 blend, although the IP offsets are the same or even smaller, indicating molecular structure and/or molecular arrangement may also help the hole transfer process besides energetic offsets. For electron transfer process, due to the large enough energetic offsets, all three blends showed

similar and fast enough electron transfer speeds. More analysis can be found in **Note 1** and **2,** Supporting Information.

After efficient charge separation, good charge transport properties are also required for high device efficiencies. Space-charge-limited current (SCLC) method was thus used to measure the hole and electron mobilities. As shown in **Figure S16** and **Table S4**, Supporting Information, PM6:BTP-S2 blend possesses the highest hole mobility (μ_h) of 12.12 × 10^{-4} cm^2 V^{-1} s^{-1} and the highest electron mobility (μ_e) of 8.29 × 10^{-4} cm^2 V^{-1} s^{-1}. As comparison, PM6:BTP-S1 blend owns the lowest μ_h of 5.19 × 10^{-4} cm^2 V^{-1} s^{-1} and the lowest μ_e of 4.16 × 10^{-4} cm^2 V^{-1} s^{-1}, while PM6:Y6 blend shows the in-between values (μ_h = 5.40 × 10^{-4} cm^2 V^{-1} s^{-1}, μ_e = 6.57 × 10^{-4} cm^2 V^{-1} s^{-1}). The relationships of mobilities among these three blends are correlated with the crystallinity and molecular orientation, which will be discussed in the following blend morphology characterization.

No matter before or after charge separation, charge recombination should be mitigated as much as possible. To understand the charge recombination situations, *J-V* curves under various light intensities (P_{light}) were measured and analyzed (**Figure S17,** Supporting Information). The relationship between J_{sc} and P_{light} can be described as $J_{sc} \propto P_{light}^{\alpha}$, in which $\alpha = 1$ represents the minimal bimolecular recombination and the relationship between V_{oc} and P_{light} can be described as $V_{oc} \propto nkT/qln(P_{light})$ (where k is the Boltzmann constant, T is the Kelvin temperature, and q is the elementary charge), in which the larger of n value represents the more proportional monomolecular recombination. It was found that PM6:Y6 blend had the least bimolecular recombination, but the most monomolecular recombination. The PM6:BTP-S1 blend had the most bimolecular recombination, but the least monomolecular recombination, while PM6:BTP-S2 blend showed the in-between situation. The charge recombination situations of these three blends related with the phase separation revealed in the following blend morphology characterization.

In the BHJ active layers, the formation of interpenetrating networks with suitable phase separation sizes is necessary for efficient device performances. Thus, to study the top surface morphology, we first performed atomic force microscopy (AFM) measurement and the results are shown in **Figure 4a** and **Figure S18,** Supporting Information. Clearly, both in the height images and phase images, we observed nanofiber-like morphology for all the three blends, indicating interpenetrating networks are all well formed in these three blends. However, there lies a big difference in phase separation sizes. Obviously, PM6:BTP-S1 blend presents the smallest domain sizes, which was beneficial for reducing monomolecular recombination, but risky for more bimolecular recombination. In contrast, PM6:Y6 blend presents the largest domain sizes, which was beneficial for reducing bimolecular recombination, but risky for more monomolecular recombination. As comparison, PM6:BTP-S2 presented the in-between situation, thus well balancing the bimolecular recombination and monomolecular recombination. The situations of top surface blend morphology are well consistent with the charge recombination demonstrated above.

Then, to study the crystallinity and molecular orientation in the blends, we performed grazing-incidence wide-angle X-ray scattering (GIWAXS) characterization.[48,49] For neat acceptors, different features are presented (**Figure 4c** and **Figure S19,** Supporting Information). BTP-S1 shows a dominant π-π stacking peak at q ≈ 1.79 $Å^{-1}$ (d = 3.51 Å) in the out-of-plane (OOP) direction, indicating a preferred face-on orientated molecular packing favorable for vertical charge transport. There are multiple scattering peaks at q ≈ 0.3 $Å^{-1}$, implying that it might have disordered lamellar packing. On the other hand, BTP-S2 and Y6 also exhibit face-on orientation with the π-π stacking peak appeared in the OOP direction, but at a relatively smaller q of 1.74 $Å^{-1}$ (d = 3.61 Å). BTP-S2 possesses a definite lamellar peak at q ≈ 0.35 $Å^{-1}$ (d = 18.0 Å) while Y6 possesses a lamellar peak at q ≈ 0.28 $Å^{-1}$ (d = 22.4 Å) and a backbone ordering peak at q ≈ 0.42 $Å^{-1}$ (d = 15.0 Å) in the in-plane direction.[7,49] In the pure film, BTP-S2 has the highest crystallinity suggested by the overall higher scattering

intensity. After blending with the donor PM6, all the three blends demonstrate similar features with a lamellar peak at 0.30 $Å^{-1}$ (d = 20.93 Å) and a strong π-π stacking peak at 1.72 $Å^{-1}$ (d = 3.65 Å) for PM6:BTP-S1 blend and 1.74 $Å^{-1}$ (d = 3.61 Å) for PM6:BTP-S2 and PM6:Y6 blends in the OOP direction (**Figure 4d**). Therefore, the π-π stacking is tighter in PM6:BTP-S2 and PM6:Y6 blends. Despite similar features in the blends, PM6:BTP-S2 blend shows higher crystallinity than those of PM6:BTP-S1 and PM6:Y6 blends, consistent with its higher mobilities than PM6:BTP-S1 and PM6:Y6 blends, as shown in the SCLC measurement.

As shown above, BTP-S2-based OPVs possess high voltages and low energy loss, while Y6-based OPVs possess high photocurrents. GIWAXS measurement shows that BTP-S2 and Y6 own similar face-on molecular orientations, thus well compatibility can be expected between BTP-S2 and Y6. Therefore, it is desirable to fabricate ternary OPVs based on PM6:Y6:BTP-S2 blend for achieving a further higher efficiency.[50-53] By keeping the total D/A weight ratio as 1:1.2, different ratios of BTP-S2 in the acceptor mixture were added to the PM6:Y6 blend. With increasing BTP-S2 ratio, the absorption in visible region become stronger for the ternary blends (**Figure S20**, Supporting Information). More fabrication details can be found in the Supporting Information. The results of ternary OPVs are displayed in **Figure 5** and **Figure S21**, Supporting Information, and the photovoltaic parameters are summarized in **Table 3**. It was found that a champion PCE of 17.43% can be realized for ternary OPVs with 20% BTP-S2 ratio, which is among the best results for single-junction OPVs. It is also exciting to find that, when the BTP-S2 ratio changes among 10% ~ 50%, all the ternary OPVs can reach over 17% efficiencies, indicating good compatibility between BTP-S2 and Y6 and broad compositional tolerance for ternary OPVs. Energy level measurement of Y6:BTP-S2 mixture (4:1, by wt.) also confirms the good compatibility between two electron acceptors, providing only one EA value of -4.07 eV and one IP value of -5.62 eV (**Figure S22,** Supporting Information). The nanoscaled phase separation with the smooth roughness for 20% BTP-S2 ternary blend film is observed (Figure S23, Supporting

Information). Compared with binary OPVs, the improvements of ternary OPVs mainly originate from Voc and FF. Especially in V_{oc}, as shown in Figure 5c, a small ratio of BTP-S2 could significantly improve the voltages of ternary OPVs, illustrating that BTP-S2 is indeed a good material in reducing energy loss. When BTP-S2 ratio increased to 50%, ternary OPVs showed an extremely high voltage of 0.9 V with over 17% efficiency maintained. Such a high voltage is very outstanding for OPVs with absorption up to 930 nm. Above results obviously demonstrate that asymmetric terminated electron acceptors are good materials for high-efficiency and low-energy-loss OPVs.

In conclusion, we report herein a new molecular designing for NFAs: asymmetric electron acceptors containing indandione and 3-dicyanomethylene-1-indanone as two different terminals. Such asymmetric electron acceptors allow us introducing six halogen atoms at the terminals, for example, BTP-S1 with four chlorine atoms and two fluorine atoms, and BTP-S2 with six chlorine atoms. We comparatively studied the energy losses and charge separation of asymmetric and symmetric NFAs. In energy loss, we found that devices based on asymmetric NFAs (BTP-S1 and BTP-S2) achieved lower non-radiative loss, thus providing higher V_{oc} than devices based on symmetric NFA (Y6). Besides, the asymmetric molecule BTP-S2 with only chlorine atoms works better than BTP-S1 with both fluorine and chlorine atoms. A high EQE_{EL} value of 2.3×10^{-2} %, corresponding to a low non-radiative loss of 0.22 eV, was realized in PM6:BTP-S2-based devices, obviously better than that (EQE_{EL} = 4.4×10^{-3} %) of PM6:Y6-based devices. In charge separation, we found that under small IP offset (< 0.2 eV), blends based on asymmetric NFAs (BTP-S1 and BTP-S2) showed faster hole transfer than blend based on symmetric NFA (Y6), while under large EA offset (> 0.3 eV), electron transfer speeds were mainly decided by the energy level offset. As a result, with both benefits in energy loss and charge separation, binary OPVs based on PM6:BTP-S1 and PM6:BTP-S2 blends exhibited high PCEs of 15.21% and 16.37%, respectively. By applying a ternary blend of PM6:Y6:BTP-S2, the best efficiency of 17.43% was realized and over 17%

efficiency could be maintained among the wide ratio range of 10 ~ 50% BTP-S2. This work provides a new design strategy for NFAs with asymmetric terminals for high-efficiency and low-energy-loss OPVs.

Supporting Information
Supporting Information is available from the Wiley Online Library or from the author.

Acknowledgements

S. L. and L. Z. contributed equally to this work. This work is supported by National Key Research and Development Program of China (No. 2019YFA0705900), the National Natural Science Foundation of China (Nos. 21734008, 21875216, 51803178, 61721005), the China Postdoctoral Science Foundation Funded Project (Nos. 2017M621907, 2019T120501) and S&T Innovation 2025 Major Special Programme of Ningbo (No. 2018B10055). X.L. and T.-K.L. acknowledge the financial support from Research Grant Council of Hong Kong (Grant No. N_CUHK418/17, General Research Fund No. 14303519, CUHK Direct Grant No. 4053304). Y.J. and F.Z. acknowledge the financial support from Swedish Government Strategic Research Area in Material Science on Functional Materials at Linköping University (Faculty Grant SFO-Mat-LiU No 200900971), Swedish Research Council (2017-04123), and China Scholarship Council (CSC).

Received: ((will be filled in by the editorial staff))
Revised: ((will be filled in by the editorial staff))
Published online: ((will be filled in by the editorial staff))

References

[1] J. Hou, O. Inganäs, R. H. Friend, F. Gao, *Nat. Mater.* **2018**, *17*, 119.
[2] C. Yan, S. Barlow, Z. Wang, H. Yan, A. K. Y. Jen, S. R. Marder, X. Zhan, *Nat. Rev. Mater.* **2018**, *3*, 18003.
[3] G. Zhang, J. Zhao, P. C. Y. Chow, K. Jiang, J. Zhang, Z. Zhu, J. Zhang, F. Huang, H. Yan, *Chem. Rev.* **2018**, *118*, 3447.
[4] H. Fu, Z. Wang, Y. Sun, *Angew. Chem. Int. Ed.* **2019**, *58*, 4442.
[5] S. Li, W. Liu, C.-Z. Li, M. Shi, H. Chen, *Small* **2017**, *13*, 1701120.
[6] Y. Lin, J. Wang, Z.-G. Zhang, H. Bai, Y. Li, D. Zhu, X. Zhan, *Adv. Mater.* **2015**, *27*, 1170.
[7] J. Yuan, Y. Zhang, L. Zhou, G. Zhang, H.-L. Yip, T.-K. Lau, X. Lu, C. Zhu, H. Peng, P. A. Johnson, M. Leclerc, Y. Cao, J. Ulanski, Y. Li, Y. Zou, *Joule* **2019**, *3*, 1140.
[8] S. Li, L. Zhan, F. Liu, J. Ren, M. Shi, C.-Z. Li, T. P. Russell, H. Chen, *Adv. Mater.* **2018**, *30*, 1705208.
[9] W. Zhao, S. Li, H. Yao, S. Zhang, Y. Zhang, B. Yang, J. Hou, *J. Am. Chem. Soc.* **2017**, *139*, 7148.

[10] S. Dai, F. Zhao, Q. Zhang, T.-K. Lau, T. Li, K. Liu, Q. Ling, C. Wang, X. Lu, W. You, X. Zhan, *J. Am. Chem. Soc.* **2017**, *139*, 1336.
[11] S. Li, L. Ye, W. Zhao, X. Liu, J. Zhu, H. Ade, J. Hou, *Adv. Mater.* **2017**, *29*, 1704051.
[12] Z.-P. Yu, Z.-X. Liu, F.-X. Chen, R. Qin, T.-K. Lau, J.-L. Yin, X. Kong, X. Lu, M. Shi, C.-Z. Li, H. Chen, *Nat. Commun.* **2019**, *10*, 2152.
[13] Y. Cui, H. Yao, J. Zhang, T. Zhang, Y. Wang, L. Hong, K. Xian, B. Xu, S. Zhang, J. Peng, Z. Wei, F. Gao, J. Hou, *Nat. Commun.* **2019**, *10*, 2515.
[14] X. Xu, K. Feng, Z. Bi, W. Ma, G. Zhang, Q. Peng, *Adv. Mater.* **2019**, *31*, 1901872.
[15] K. Jiang, Q. Wei, J. Y. L. Lai, Z. Peng, H. K. Kim, J. Yuan, L. Ye, H. Ade, Y. Zou, H. Yan, *Joule* **2019**, *3*, 3020.
[16] Y. Lin, B. Adilbekova, Y. Firdaus, E. Yengel, H. Faber, M. Sajjad, X. Zheng, E. Yarali, A. Seitkhan, O. M. Bakr, A. El-Labban, U. Schwingenschlögl, V. Tung, I. McCulloch, F. Laquai, T. D. Anthopoulos, *Adv. Mater.* **2019**, *31*, 1902965.
[17] Y. Cui, H. Yao, L. Hong, T. Zhang, Y. Tang, B. Lin, K. Xian, B. Gao, C. An, P. Bi, W. Ma, J. Hou, *Natl. Sci. Rev.* **2019**, DOI: 10.1093/nsr/nwz200.
[18] S. Liu, J. Yuan, W. Deng, M. Luo, Y. Xie, Q. Liang, Y. Zou, Z. He, H. Wu, Y. Cao, *Nat. Photonics* **2020**, DOI: 10.1038/s41566-019-0573-5.
[19] L. Zhan, S. Li, T.-K. Lau, Y. Cui, X. Lu, M. Shi, C.-Z. Li, H. Li, J. Hou, H. Chen, *Energy Environ. Sci.* **2020**, *13*, 635.
[20] V. Coropceanu, X.-K. Chen, T. Wang, Z. Zheng, J.-L. Brédas, *Nat. Rev. Mater.* **2019**, *4*, 689.
[21] J. Liu, S. Chen, D. Qian, B. Gautam, G. Yang, J. Zhao, J. Bergqvist, F. Zhang, W. Ma, H. Ade, O. Inganäs, K. Gundogdu, F. Gao, H. Yan, *Nat. Energy* **2016**, *1*, 16089.
[22] S. Li, L. Zhan, C. Sun, H. Zhu, G. Zhou, W. Yang, M. Shi, C.-Z. Li, J. Hou, Y. Li, H. Chen, *J. Am. Chem. Soc.* **2019**, *141*, 3073.
[23] P. K. Nayak, S. Mahesh, H. J. Snaith, D. Cahen, *Nat. Rev. Mater.* **2019**, *4*, 269.
[24] D. Qian, Z. Zheng, H. Yao, W. Tress, T. R. Hopper, S. Chen, S. Li, J. Liu, S. Chen, J. Zhang, X.-K. Liu, B. Gao, L. Ouyang, Y. Jin, G. Pozina, I. A. Buyanova, W. M. Chen, O. Inganäs, V. Coropceanu, J.-L. Bredas, H. Yan, J. Hou, F. Zhang, A. A. Bakulin, F. Gao, *Nat. Mater.* **2018**, *17*, 703.
[25] T. J. Aldrich, M. Matta, W. Zhu, S. M. Swick, C. L. Stern, G. C. Schatz, A. Facchetti, F. S. Melkonyan, T. J. Marks, *J. Am. Chem. Soc.* **2019**, *141*, 3274.
[26] H. Zhang, H. Yao, J. Hou, J. Zhu, J. Zhang, W. Li, R. Yu, B. Gao, S. Zhang, J. Hou, *Adv. Mater.* **2018**, *30*, 1800613.
[27] H. Chen, Z. Hu, H. Wang, L. Liu, P. Chao, J. Qu, W. Chen, A. Liu, F. He, *Joule* **2018**, *2*, 1623.
[28] H. Chen, D. Hu, Q. Yang, J. Gao, J. Fu, K. Yang, H. He, S. Chen, Z. Kan, T. Duan, C. Yang, J. Ouyang, Z. Xiao, K. Sun, S. Lu, *Joule* **2019**, *3*, 3034.
[29] W. Li, L. Ye, S. Li, H. Yao, H. Ade, J. Hou, *Adv. Mater.* **2018**, *30*, 1707170.
[30] H. Yao, Y. Cui, D. Qian, C. S. Ponseca, A. Honarfar, Y. Xu, J. Xin, Z. Chen, L. Hong, B. Gao, R. Yu, Y. Zu, W. Ma, P. Chabera, T. Pullerits, A. Yartsev, F. Gao, J. Hou, *J. Am. Chem. Soc.* **2019**, *141*, 7743.
[31] H. Yao, Y. Cui, R. Yu, B. Gao, H. Zhang, J. Hou, *Angew. Chem. Int. Ed.* **2017**, *56*, 3045.
[32] S. M. Menke, N. A. Ran, G. C. Bazan, R. H. Friend, *Joule* **2018**, *2*, 25.
[33] Y. Cui, Y. Wang, J. Bergqvist, H. Yao, Y. Xu, B. Gao, C. Yang, S. Zhang, O. Inganäs, F. Gao, J. Hou, *Nat. Energy* **2019**, *4*, 768.
[34] F. D. Eisner, M. Azzouzi, Z. Fei, X. Hou, T. D. Anthopoulos, T. J. S. Dennis, M. Heeney, J. Nelson, *J. Am. Chem. Soc.* **2019**, *141*, 6362.
[35] L. Zhan, S. Li, H. Zhang, F. Gao, T.-K. Lau, X. Lu, D. Sun, P. Wang, M. Shi, C.-Z. Li, H. Chen, *Adv. Sci.* **2018**, *5*, 1800755.
[36] C. Li, H. Fu, T. Xia, Y. Sun, *Adv. Energy Mater.* **2019**, *9*, 1900999.

[37] W. Gao, M. Zhang, T. Liu, R. Ming, Q. An, K. Wu, D. Xie, Z. Luo, C. Zhong, F. Liu, F. Zhang, H. Yan, C. Yang, *Adv. Mater.* **2018**, *30*, 1800052.
[38] S. Feng, C. e. Zhang, Y. Liu, Z. Bi, Z. Zhang, X. Xu, W. Ma, Z. Bo, *Adv. Mater.* **2017**, *29*, 1703527.
[39] S. Li, L. Zhan, T.-K. Lau, Z.-P. Yu, W. Yang, T. R. Andersen, Z. Fu, C.-Z. Li, X. Lu, M. Shi, H. Chen, *Small Methods* **2019**, *3*, 1900531.
[40] S. Li, L. Zhan, W. Zhao, S. Zhang, B. Ali, Z. Fu, T.-K. Lau, X. Lu, M. Shi, C.-Z. Li, J. Hou, H. Chen, *J. Mater. Chem. A* **2018**, *6*, 12132.
[41] J. Yao, T. Kirchartz, M. S. Vezie, M. A. Faist, W. Gong, Z. He, H. Wu, J. Troughton, T. Watson, D. Bryant, J. Nelson, *Phys. Rev. Appl.* **2015**, *4*, 014020.
[42] Y. Wang, D. Qian, Y. Cui, H. Zhang, J. Hou, K. Vandewal, T. Kirchartz, F. Gao, *Adv. Energy Mater.* **2018**, *8*, 1801352.
[43] C. Sun, S. Qin, R. Wang, S. Chen, F. Pan, B. Qiu, Z. Shang, L. Meng, C. Zhang, M. Xiao, C. Yang, Y. Li, *J. Am. Chem. Soc.* **2020**, *142*, 1465.
[44] R. Qin, D. Wang, G. Zhou, Z.-P. Yu, S. Li, Y. Li, Z.-X. Liu, H. Zhu, M. Shi, X. Lu, C.-Z. Li, H. Chen, *J. Mater. Chem. A* **2019**, *7*, 27632.
[45] Z.-P. Yu, X. Li, C. He, D. Wang, R. Qin, G. Zhou, Z.-X. Liu, T. R. Andersen, H. Zhu, H. Chen, C.-Z. Li, *Chinese Chem. Lett.* **2019**, DOI: 10.1016/j.cclet.2019.12.003.
[46] H. Bin, L. Gao, Z.-G. Zhang, Y. Yang, Y. Zhang, C. Zhang, S. Chen, L. Xue, C. Yang, M. Xiao, Y. Li, *Nat. Commun.* **2016**, *7*, 13651.
[47] Z. Zhou, W. Liu, G. Zhou, M. Zhang, D. Qian, J. Zhang, S. Chen, S. Xu, C. Yang, F. Gao, H. Zhu, F. Liu, X. Zhu, *Adv. Mater.* **2020**, *32*, 1906324.
[48] J. Mai, T.-K. Lau, J. Li, S.-H. Peng, C.-S. Hsu, U. S. Jeng, J. Zeng, N. Zhao, X. Xiao, X. Lu, *Chem. Mater.* **2016**, *28*, 6186.
[49] J. Mai, Y. Xiao, G. Zhou, J. Wang, J. Zhu, N. Zhao, X. Zhan, X. Lu, *Adv. Mater.* **2018**, *30*, 1802888.
[50] L. Zhan, S. Li, S. Zhang, T.-K. Lau, T. R. Andersen, X. Lu, M. Shi, C.-Z. Li, G. Li, H. Chen, *Sol. RRL* **2019**, *3*, 1900317.
[51] L. Zhan, S. Li, S. Zhang, X. Chen, T.-K. Lau, X. Lu, M. Shi, C.-Z. Li, H. Chen, *ACS Appl. Mater. Interfaces* **2018**, *10*, 42444.
[52] N. Gasparini, A. Salleo, I. McCulloch, D. Baran, *Nat. Rev. Mater.* **2019**, *4*, 229.
[53] Z. Zhou, S. Xu, J. Song, Y. Jin, Q. Yue, Y. Qian, F. Liu, F. Zhang and X. Zhu, *Nat. Energy*, **2018**, *3*, 952.

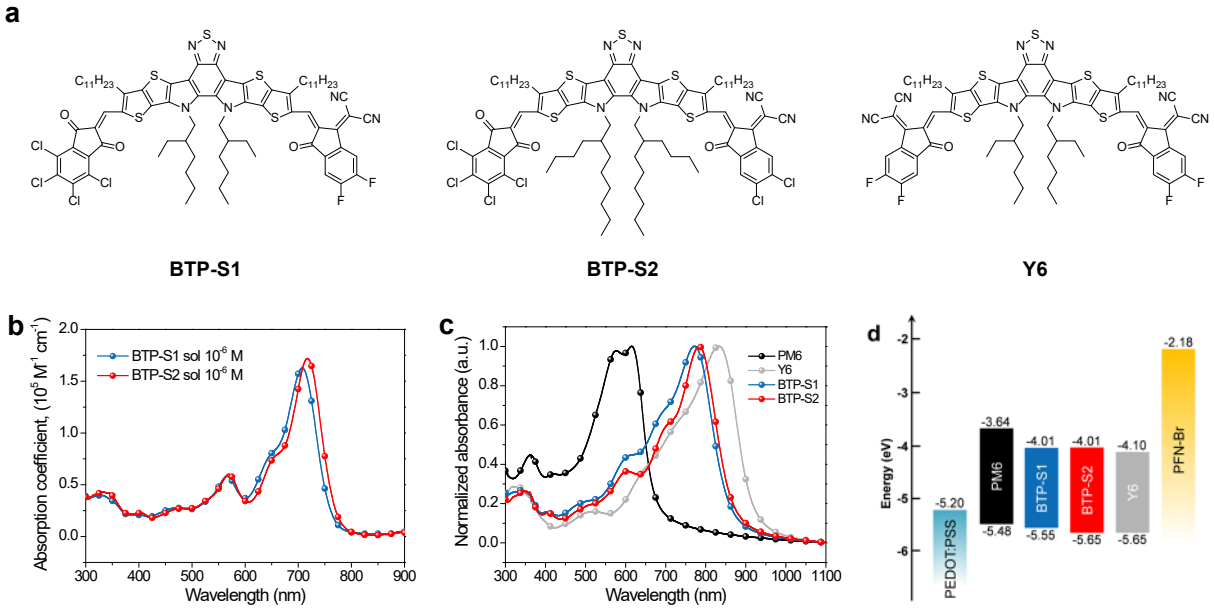

Figure 1. a) Chemical structures of BTP-S1, BTP-S2 and Y6. b) Absorption spectra of BTP-S1 and BTP-S2 in 10^{-6} M chloroform solutions. c) Normalized absorption spectra of PM6, Y6, BTP-S1 and BTP-S2 thin films. d) Schematic energy level alignment of the studied materials.

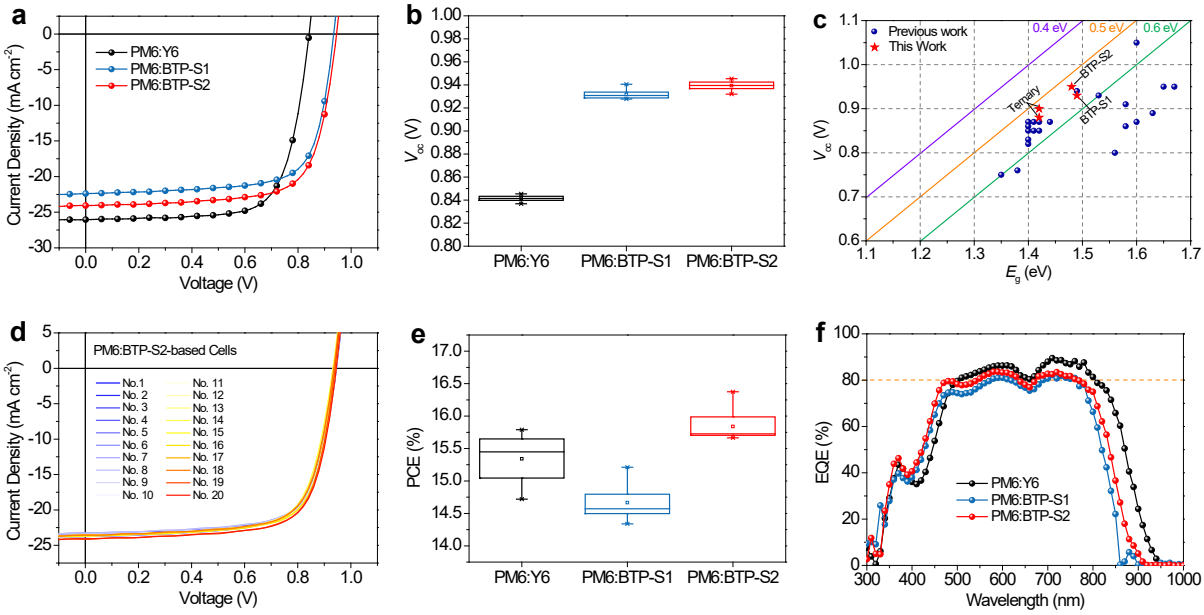

Figure 2. a) *J-V* curves of OPVs based on PM6:BTP-S1, PM6:BTP-S2, and PM6:Y6 blends. b) Statistics of V_{oc} for PM6:BTP-S1, PM6:BTP-S2, and PM6:Y6-based OPVs. c) Comparison of energy loss between this work and previous works (original data are summarized in Table S3, Supporting Information). d) *J-V* curves of 20 independent OPVs based on PM6:BTP-S2 blend. e) Statistics of PCEs for PM6:BTP-S1-, PM6:BTP-S2-, and PM6:Y6-based OPVs. f) EQE curves of relevant OPVs.

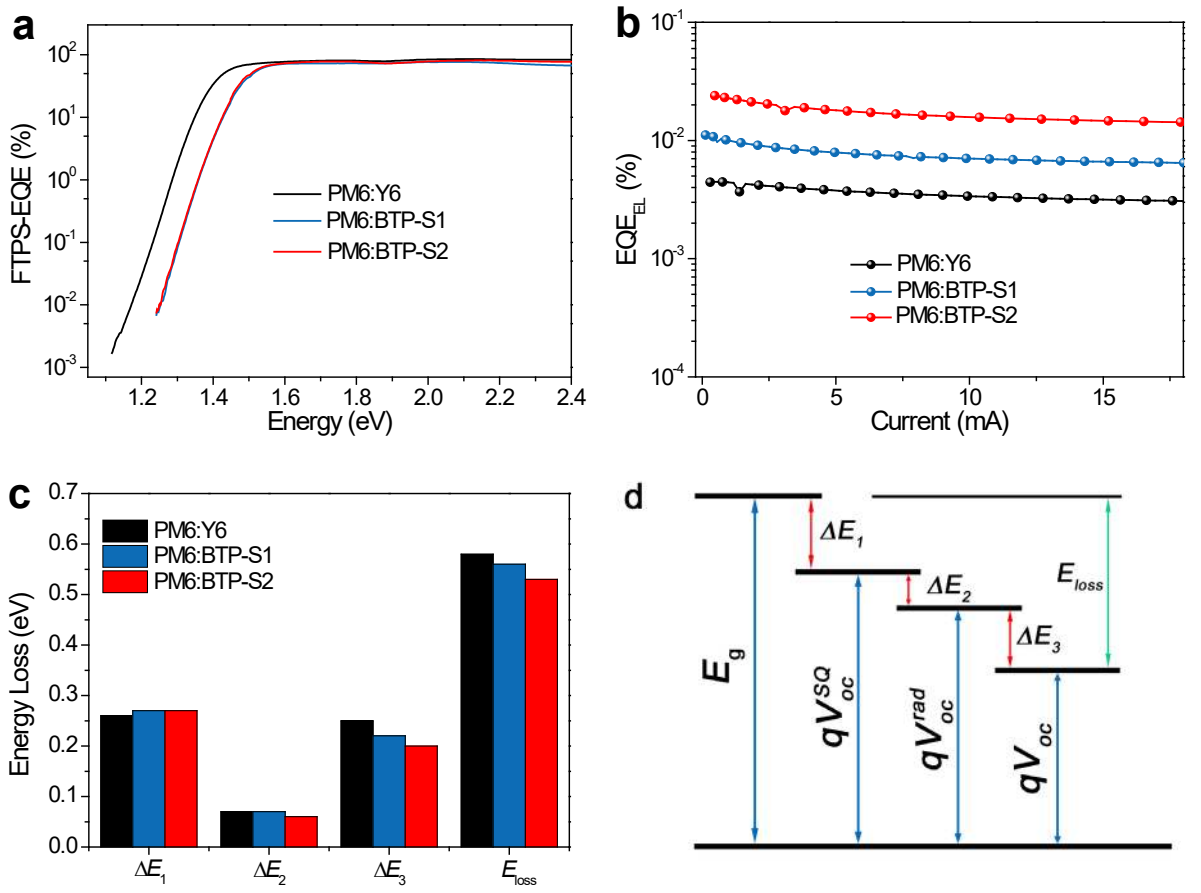

Figure 3. a) FTPS curves of OPVs based on PM6:Y6, PM6:BTP-S1 and PM6:BTP-S2 blends. b) EQE_{EL} of OPVs at various injected currents. c) Comparison of radiative and non-radiative energy losses in three types of OPVs. d) Diagram of different parts of energy losses.

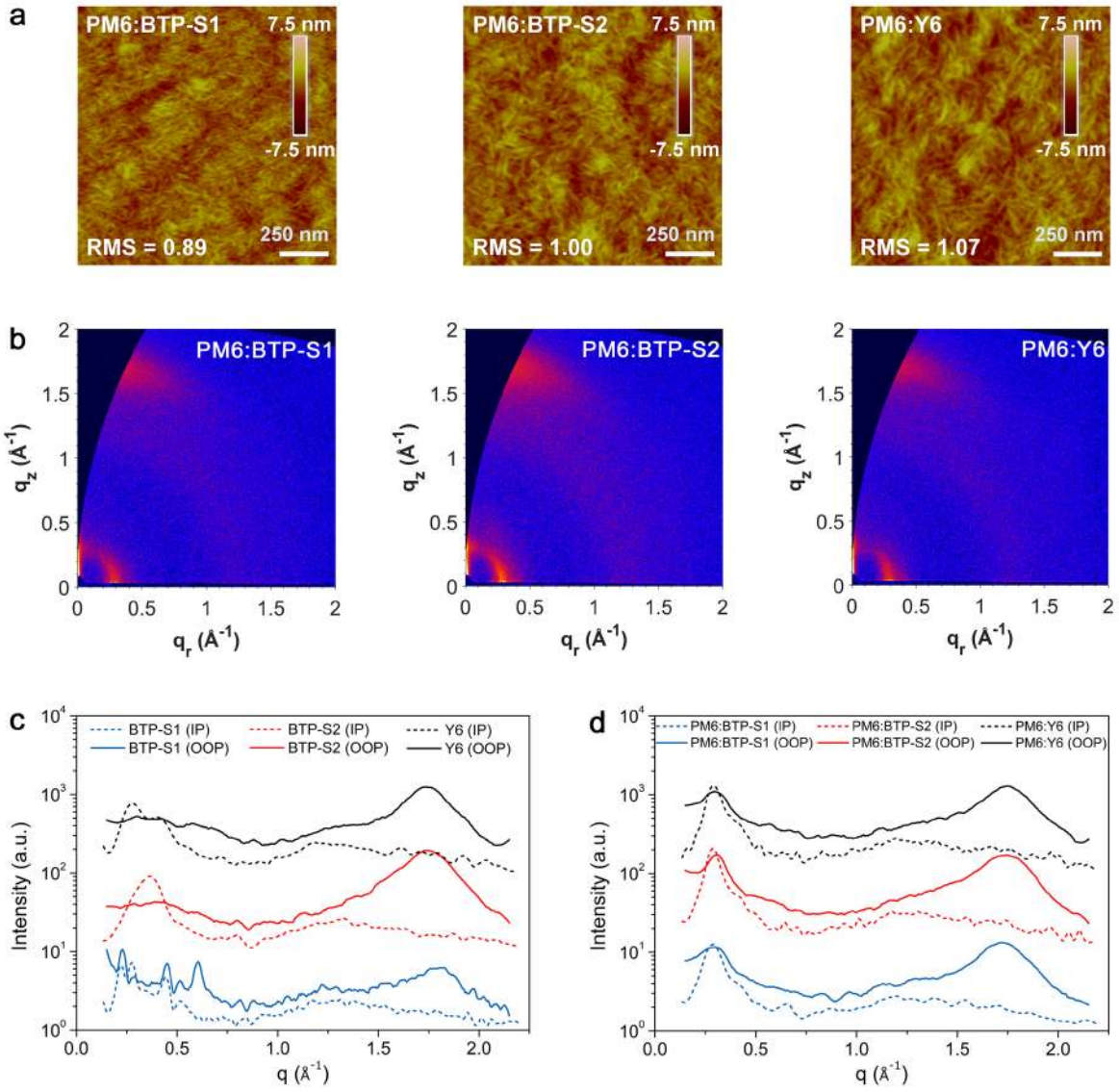

Figure 4. a) AFM height images of PM6:BTP-S1, PM6:BTP-S2 and PM6:Y6 blends. b) 2D GIWAXS images of PM6:BTP-S1, PM6:BTP-S2 and PM6:Y6 blends. c) 1D intensity profiles of BTP-S1, BTP-S2 and Y6 films. d) 1D intensity profiles of PM6:BTP-S1, PM6:BTP-S2 and PM6:Y6 blends.

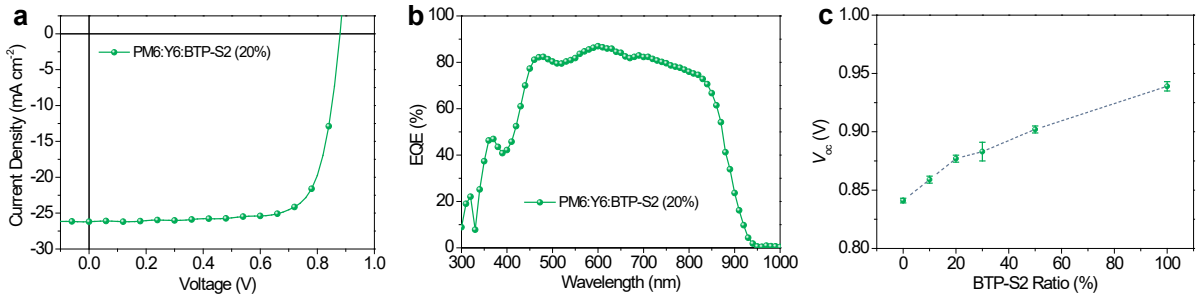

Figure 5. a) *J-V* curve of the champion ternary OPV (20% BTP-S2 in the acceptor mixture). b) EQE spectrum of the relevant OPV. c) Variation of V_{oc} with the change of BTP-S2 ratio in the acceptor mixture.

Table 1. Photovoltaic parameters of the OPVs based on PM6:Y6, PM6:BTP-S1 and PM6:BTP-S2 blends.

Blend	V_{oc} (V)	J_{sc} (mA cm^{-2})	FF (%)	PCE (%)[a)]
PM6:Y6	0.842 (0.841 ± 0.002)	26.05 (25.67 ± 0.32)	72.03 (71.01 ± 1.18)	15.79 (15.34 ± 0.35)
PM6:BTP-S1	0.934 (0.932 ± 0.003)	22.39 (22.22 ± 0.31)	72.69 (70.88 ± 1.31)	15.21 (14.67 ± 0.24)
PM6:BTP-S2	0.945 (0.939 ± 0.004)	24.07 (23.61 ± 0.22)	72.02 (71.41 ± 0.55)	16.37 (15.84 ± 0.21)

[a)] The average parameters were calculated from 20 independent cells.

Table 2. Detailed energy losses of OPVs based on PM6:Y6, PM6:BTP-S1 and PM6:BTP-S2 blends

Devices	E_g (eV)	qV_{oc} (eV)	E_{loss} (eV)	qV_{oc}^{SQ} (eV)	ΔE_1 (eV)	qV_{oc}^{rad} (eV)	ΔE_2 (eV)	ΔE_3 (eV)	EQE_{EL} (%)	(Exp.) $q\Delta V_{oc}^{non-rad}$ (eV)
PM6:Y6	1.42	0.84	0.58	1.16	0.26	1.09	0.07	0.25	4.4×10^{-3}	0.26
PM6:BTP-S1	1.49	0.93	0.56	1.22	0.27	1.15	0.07	0.22	1.1×10^{-2}	0.24
PM6:BTP-S2	1.48	0.95	0.53	1.21	0.27	1.15	0.06	0.20	2.3×10^{-2}	0.22

Table 3. Photovoltaic parameters of the ternary OPVs based on PM6:Y6:BTP-S2 blends with various BTP-S2 ratios

BTP-S2 Ratio[a)]	V_{oc} (V)	J_{sc} (mA cm^{-2})	FF (%)	PCE (%)
0%	0.842 (0.841 ± 0.002)	26.05 (25.67 ± 0.32)	72.03 (71.01 ± 1.18)	15.79 (15.34 ± 0.35)
10%	0.861 (0.859 ± 0.003)	26.94 (26.54 ± 0.32)	74.44 (74.35 ± 0.99)	17.23 (16.91 ± 0.21)
20%	0.880 (0.877 ± 0.003)	26.20 (26.04 ± 0.21)	75.80 (74.78 ± 0.74)	17.43 (17.03 ± 0.21)
30%	0.884 (0.883 ± 0.008)	26.07 (26.08 ± 0.33)	74.67 (73.87 ± 0.80)	17.16 (16.97 ± 0.13)
50%	0.897 (0.902 ± 0.003)	26.11 (25.76 ± 0.31)	73.02 (72.53 ± 0.66)	17.06 (16.81 ± 0.16)

[a)] Weight ratio of BTP-S2 in the acceptor mixture (total D/A ratio is kept as 1:1.2).

Supporting Information

Asymmetric Electron Acceptors for High-Efficiency and Low-Energy-Loss Organic Photovoltaics

Shuixing Li, Lingling Zhan, Yingzhi Jin, Guanqing Zhou, Tsz-Ki Lau, Ran Qin, Minmin Shi, Chang-Zhi Li, Haiming Zhu, Xinhui Lu, Fengling Zhang,* and Hongzheng Chen**

S. Li and L. Zhan contributed equally to this work.

Dr. S. Li, Dr. L. Zhan, R. Qin, Prof. M. Shi, Prof. C.-Z. Li, Prof. H. Chen
State Key Laboratory of Silicon Materials, MOE Key Laboratory of Macromolecular Synthesis and Functionalization, Department of Polymer Science and Engineering, Zhejiang University, 310027 Hangzhou, P. R. China
E-mail: minminshi@zju.edu.cn, hzchen@zju.edu.cn
Y. Jin, Prof. F. Zhang
Department of Physics, Chemistry and Biology (IFM), Linköping University, 581 83 Linköping, Sweden.
E-mail: fengling.zhang@liu.se
Prof. H. Zhu
Department of Chemistry, Zhejiang University, 310027 Hangzhou, P. R. China.
Dr. T.-K. Lau, Prof. X. Lu
Department of Physics, Chinese University of Hong Kong, New Territories, 999077 Hong Kong, P. R. China.
G. Zhou
School of Chemistry and Chemical Engineering, and Center for Advanced Electronic Materials and Devices, Shanghai Jiao Tong University, 200240 Shanghai, P. R. China.

Materials Synthesis

Synthesis of BTP-S1, BTP-S2 and BTP-S3.

Note: Compound **1**, Compound **3**, Compound **5**, Compound **6** and Compound **8** were purchased from commercial companies and used without further purifications (Derthon Inc.).

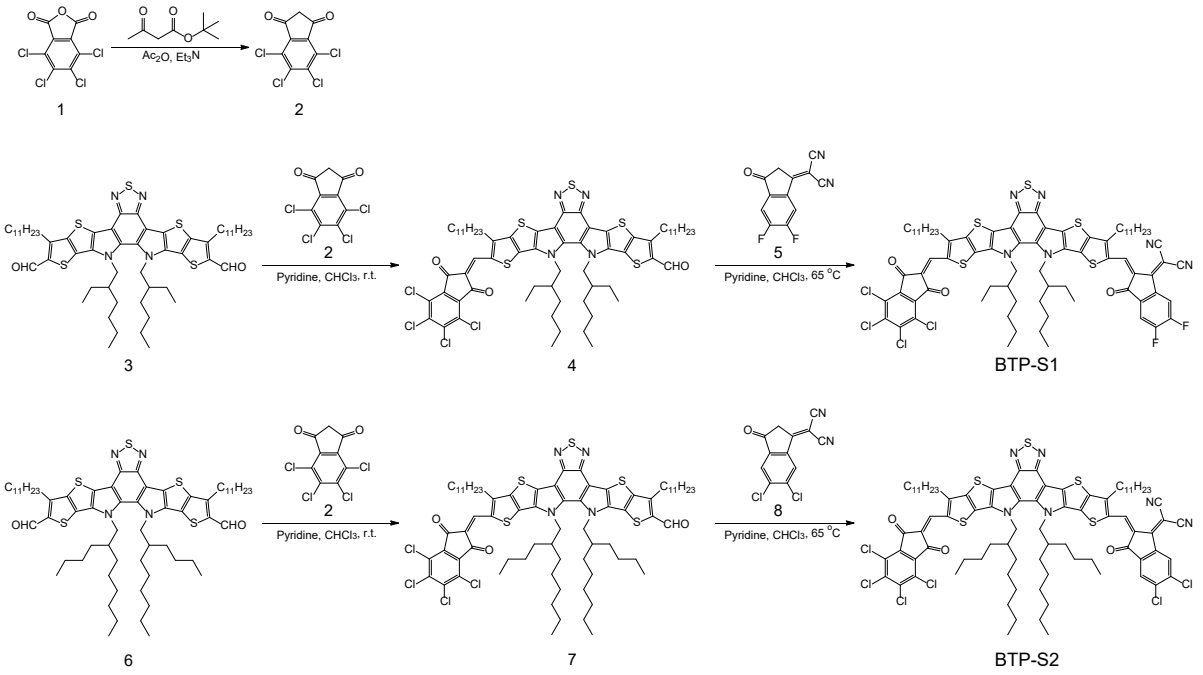

4,5,6,7-tetrachloro-1H-indene-1,3(2H)-dione (**Compound 2**)

To a two-necked round-bottom flask were added **Compound 1** (2.86 g, 10 mmol), Ac_2O (10 mL) and Et_3N (5 mL). The mixture was frozen with liquid nitrogen, followed by three times of successive vacuum and nitrogen fill cycles. Then, under the protection of N_2, *tert*-butyl 3-oxobutanoate (1.7 mL, 10 mmol) was injected to the reactant. Then the mixture was stirred at room temperature for 12 h. After that, the mixture of ice water and conc. HCl (12 mL, 1:1, v/v) was slowly injected and the reactant was stirred for 0.5 h. Then, 16 mL conc. HCl was further added slowly and the mixture was refluxed at 70 ºC for 2 h. After cooling, the mixture was pouring into the water, extracted with chloroform and dried with anhydrous $MgSO_4$. After removing the solvent, silica gel column chromatography was used to purify the product with the mixture of dichloromethane and methanol (50:1, v/v) as the eluent, yielding a grey white solid (1.14 g, 40%). ^{1}H NMR (400 MHz, $CDCl_3$): δ = 3.38 (s, 2H). ^{13}C NMR (400 MHz, $CDCl_3$): δ = 191.40, 141.82, 137.70, 129.78, 45.59.

12,13-bis(2-ethylhexyl)-10-((4,5,6,7-tetrachloro-1,3-dioxo-1,3-dihydro-2H-inden-2-ylidene)methyl)-3,9-diundecyl-12,13-dihydro-[1,2,5]thiadiazolo[3,4-e]thieno[2'',3'':4',5']thieno[2',3':4,5]pyrrolo[3,2-g]thieno[2',3':4,5]thieno[3,2-b]indole-2-carbaldehyde (**Compound 4**)

To a Schlenk tube were added **Compound 3** (0.25 g, 0.25 mmol), **Compound 2** (0.14 g, 0.5 mmol) and $CHCl_3$ (40 mL). The mixture was frozen with liquid nitrogen, followed by three times of successive vacuum and nitrogen fill cycles. Then, under the protection of N_2, 0.6 mL

pyridine was injected. The reactant was stirred at room temperature (~ 30 °C) for 5h. The crude product was purified on silica gel column chromatography with the mixture of petroleum ether and dichloromethane (1:1, v/v) as the eluent, yielding a brown solid (0.22 g, 68%). ^{1}H NMR (400 MHz, $CDCl_3$): δ = 10.16 (s, 1H), 8.26 (s, 1H), 4.84-4.63 (m, 4H), 3.27-3.12 (m, 4H), 2.15-2.01 (m, 2H), 1.98-1.82 (m, 4H), 1.53-1.43 (m, 4H), 1.42-1.34 (m, 4H), 1.33-1.11 (m, 28H), 1.08-0.80 (m, 18H), 0.77-0.57 (m, 12H).

(Z)-2-(2-((12,13-bis(2-ethylhexyl)-10-((4,5,6,7-tetrachloro-1,3-dioxo-1,3-dihydro-2H-inden-2-ylidene)methyl)-3,9-diundecyl-12,13-dihydro-[1,2,5]thiadiazolo[3,4-e]thieno[2'',3'':4',5']thieno[2',3':4,5]pyrrolo[3,2-g]thieno[2',3':4,5]thieno[3,2-b]indol-2-yl)methylene)-5,6-difluoro-3-oxo-2,3-dihydro-1H-inden-1-ylidene)malononitrile (**BTP-S1**)

To a Schlenk tube were added **Compound 4** (0.22 g, 0.17 mmol), **Compound 5** (0.12 g, 0.52 mmol) and $CHCl_3$ (40 mL). The mixture was frozen with liquid nitrogen, followed by three times of successive vacuum and nitrogen fill cycles. Then, under the protection of N_2, 1 mL pyridine was injected. The reactant was refluxed at 65 °C for 6 h. After that, silica gel column chromatography was used to purify the product with the mixture of petroleum ether and chloroform (1:1, v/v) as the eluent, yielding a deep brown solid (0.2 g, 76%). ^{1}H NMR (400 MHz, $CDCl_3$): δ = 9.15 (s, 1H), 8.56 (dd, *J* = 9.9, 6.6 Hz, 1H), 8.26 (s, 1H), 7.72 (t, *J* = 7.5 Hz, 1H), 4.88-4.68 (m, 4H), 3.30-3.12 (m, 4H), 2.19-2.03 (m, 2H), 1.94-1.80 (m, 4H), 1.53-1.43 (m, 4H), 1.44-1.34 (m, 4H), 1.33-1.11 (m, 28H), 1.10-0.93 (m, 10H), 0.91-0.81 (m, 8H), 0.80-0.57 (m, 12H). ^{19}F NMR (400 MHz, $CDCl_3$): δ = -123.04 (d, *J* = 19.4 Hz), -124.33 (d, *J* = 19.3 Hz). MS (MALDI-TOF): Calcd for $C_{79}H_{84}Cl_4F_2N_6O_3S_5$ (M^+): 1505.68, Found: 1505.77.

12,13-bis(2-butyloctyl)-10-((4,5,6,7-tetrachloro-1,3-dioxo-1,3-dihydro-2H-inden-2-ylidene)methyl)-3,9-diundecyl-12,13-dihydro-[1,2,5]thiadiazolo[3,4-e]thieno[2'',3'':4',5']thieno[2',3':4,5]pyrrolo[3,2-g]thieno[2',3':4,5]thieno[3,2-b]indole-2-carbaldehyde (**Compound 7**)

To a Schlenk tube were added **Compound 6** (0.28 g, 0.25 mmol), **Compound 2** (0.14 g, 0.5 mmol) and $CHCl_3$ (40 mL). The mixture was frozen with liquid nitrogen, followed by three times of successive vacuum and nitrogen fill cycles. Then, under the protection of N_2, 0.6 mL pyridine was injected. The reactant was stirred at room temperature (~ 30 °C) for 5h. The crude product was purified on silica gel column chromatography with the mixture of petroleum ether and dichloromethane (1:1, v/v) as the eluent, yielding a brown solid (0.15 g, 44%). ^{1}H NMR (400 MHz, $CDCl_3$): δ = 10.09 (s, 1H), 8.16 (d, *J* = 7.4 Hz, 1H), 4.75-4.56 (m, 4H), 3.19-3.05 (m, 4H), 2.13-1.97 (m, 2H), 1.91-1.73 (m, 4H), 1.46-1.35 (m, 4H), 1.34-1.26 (m, 4H), 1.25-1.13 (m, 28H), 1.08-0.73 (m, 34H), 0.66-0.51 (m, 12H).

(Z)-2-(2-((12,13-bis(2-butyloctyl)-10-((4,5,6,7-tetrachloro-1,3-dioxo-1,3-dihydro-2H-inden-2-ylidene)methyl)-3,9-diundecyl-12,13-dihydro-[1,2,5]thiadiazolo[3,4-e]thieno[2'',3'':4',5']thieno[2',3':4,5]pyrrolo[3,2-g]thieno[2',3':4,5]thieno[3,2-b]indol-2-yl)methylene)-5,6-dichloro-3-oxo-2,3-dihydro-1H-inden-1-ylidene)malononitrile (**BTP-S2**)

To a Schlenk tube were added **Compound 7** (0.15g, 0.11 mmol), **Compound 8** (0.09 g, 0.34 mmol) and $CHCl_3$ (40 mL). The mixture was frozen with liquid nitrogen, followed by three times of successive vacuum and nitrogen fill cycles. Then, under the protection of N_2, 1 mL

pyridine was injected. The reactant was refluxed at 65 °C for 6 h. After that, silica gel column chromatography was used to purify the product with the mixture of petroleum ether and chloroform (1:1, v/v) as the eluent, yielding a deep brown solid (0.12 g, 66%). ^{1}H NMR (400 MHz, $CDCl_3$): δ = 9.16 (s, 1H), 8.77 (s, 1H), 8.26 (s, 1H), 7.96 (s, 1H), 4.89-4.67 (m, 4H), 3.30-3.11 (m, 4H), 2.23-2.08 (m, 2H), 1.95-1.79 (m, 4H), 1.54-1.44 (m, 4H), 1.43-1.34 (m, 4H), 1.33-1.17 (m, 28H), 1.15-0.76 (m, 34H), 0.74-0.60 (m, 12H). MS (MALDI-TOF): Calcd for $C_{87}H_{100}Cl_6N_6O_3S_5$ (M^+): 1650.80, Found: 1650.37.

2,2'-((12,13-bis(2-butyloctyl)-3,9-diundecyl-12,13-dihydro-[1,2,5]thiadiazolo[3,4-e]thieno[2'',3'':4',5']thieno[2',3':4,5]pyrrolo[3,2-g]thieno[2',3':4,5]thieno[3,2-b]indole-2,10-diyl)bis(methanylylidene))bis(4,5,6,7-tetrachloro-1H-indene-1,3(2H)-dione) (**BTP-S3**)

BTP-S3 (see chemical structure in **Figure S1**) was separated as a pure material during the step of synthesizing **Compound 7**. ^{1}H NMR (400 MHz, $CDCl_3$): δ = 8.28 (s, 2H), 4.87-4.71 (m, 4H), 3.28-3.16 (m, 4H), 2.20-2.09 (m, 2H), 1.95-1.83 (m, 4H), 1.53-1.44 (m, 4H), 1.43-1.34 (m, 4H), 1.33-1.21 (m, 28H), 1.14-0.81 (m, 34H), 0.74-0.59 (m, 12H). MS (MALDI-TOF): Calcd for $C_{84}H_{98}Cl_8N_4O_4S_5$ (M^+): 1671.63, Found: 1671.29.

Supporting Methods

General Characterizations. ^{1}H NMR spectra were obtained on a Bruker Advance III 400 (400 MHz) nuclear magnetic resonance (NMR) spectroscope. MALDI-TOF MS spectra were measured on a Walters Maldi Q-TOF Premier mass spectrometry. UV-vis-NIR absorption spectra were recorded on a Shimadzu UV-1800 spectrophotometer. Cyclic voltammetry (CV) was done on a CHI600A electrochemical workstation with Pt disk, Pt plate, and standard calomel electrode (SCE) as working electrode, counter electrode, and reference electrode, respectively, in a 0.1 mol/L tetrabutylammoniumhexafluorophosphate (Bu_4NPF_6) acetonitrile solution. The CV curves were recorded versus the potential of SCE, which was calibrated by the ferrocene-ferrocenium (Fc/Fc^+) redox couple (4.8 eV below the vacuum level). The equation of $E_{EA/IP}$ = -e($E_{red/ox}$+4.41) (eV) was used to calculate the EA and IP levels (the redox potential of Fc/Fc^+ is found to be 0.39 V). AFM images were obtained on a VeecoMultiMode atomic force microscopy in the tapping mode.

Device Fabrication and Measurement. Organic photovoltaics (OPVs) were fabricated on glass substrates commercially pre-coated with a layer of ITO with the conventional structure of ITO/PEDOT:PSS/Active Layer/PFN-Br/Ag. Prior to fabrication, the substrates were cleaned using detergent, deionized water, acetone and isopropanol consecutively for 15 min in each step, and then treated in an ultraviolet ozone generator for 15 min before being spin-coated at 4500 rpm with a layer of 20 nm thick PEDOT:PSS (Baytron P AI4083). After baking the PEDOT:PSS layer in air at 170 ºC for 20 min, the substrates were transferred to a glovebox. The active layer was spin-coated from chloroform solution (For PM6:BTP-S1, 16 mg/mL, D:A = 1:1, 0.8% CN. For PM6:BTP-S2, 18 mg/mL, D:A = 1:1.2, 0.5% CN. For PM6:Y6, 17.6 mg/mL, D:A = 1:1.2, 0.5% CN.) at 4000 rpm for 30 s to form the active layer. Then an extra pre-annealing at 100 ºC (PM6:BTP-S1 and PM6:Y6) or 115 ºC (PM6:BT-S2) for 10 min was performed. Then a 5 nm thick PFN-Br film was deposited as the cathode buffer layer by the spin-coating of a solution of 0.5 mg/mL PFN-Br in methanol. Finally, the Ag (100 nm) electrode was deposited by thermal evaporation to complete the device with an active area of 4 mm^2.

For the fabrication of ternary OPVs, similar procedures to the binary OPVs explained above were applied, but the active layer was replaced with a ternary blend. For the ternary blend, the total D/A weight ratio was kept as 1:1.2 with a total concentration of 17.6 mg/mL, and different ratios of BTP-S2 in the acceptor mixture were added to the PM6:Y6 blend. 0.5% CN was also added as the additive in the ternary blends. Besides, an extra pre-annealing at 100 ºC for 10 min was also performed.

Mobility Measurement. The charge carrier mobilities of the blend films were measured using the space-charge-limited current (SCLC) method. Hole-only devices were fabricated in a structure of indium tin oxide (ITO)/PEDOT:PSS/Active Layer/MoO_3/Ag. Electron-only devices were fabricated in a structure of ITO/ZnO/Active Layer/PFN-Br/Ag. The device characteristics were extracted by modeling the dark current under forward bias using the SCLC expression described by the Mott-Gurney law:

$$J = \frac{9}{8}\varepsilon_r\varepsilon_0\mu\frac{V^2}{L^3} \quad (1)$$

Here, $\varepsilon_r \approx 3$ is the average dielectric constant of the blend film, ε_0 is the permittivity of the free space, μ is the carrier mobility, L is the thickness of the film, and V is the applied voltage.

Electroluminescence Measurement. An external current/voltage source was employed to provide an external electric field to the pristine and blended solar cells. The electroluminescence emissions were recorded with an Andor spectrometer.

FTPS-EQE Measurement. The FTPS-EQE was measured with a Vertex 70 from Bruker Optics, which was equipped with a quartz tungsten halogen lamp, quartz beam-splitter and external detector option. A low-noise current amplifier (SR570) was used to amplify the photocurrent produced under illumination of the solar cells, with light modulated by the Fourier transform infrared spectroscope (FTIR). The output voltage of the current amplifier was fed back into the external detector port of the FTIR to use the FTIR software to collect the photocurrent spectra.

EQE_{EL} Measurement. The EQE_{EL} was recorded with an in-house-built system comprising a Hamamatsu silicon photodiode 1010B, Keithley 2400 source meter (for supplying voltages and recording injected currents), and Keithley 485 picoammeter (for measuring the emitted light intensity).

Transient Absorption Spectroscopy (TAS) Measurement. For femtosecond transient absorption spectroscopy, the fundamental output from Yb:KGW laser (1030 nm, 220 fs Gaussian fit, 100 kHz, Light Conversion Ltd) was separated to two light beam. One was introduced to NOPA (ORPHEUS-N, Light Conversion Ltd) to produce a certain wavelength for pump beam (here we use 750 nm), the other was focused onto a YAG plate to generate white light continuum as probe beam. The pump and probe overlapped on the sample at a small angle less than 10°. The transmitted probe light from sample was collected by a linear CCD array. Then we obtained transient differential transmission signals by equation shown below:

$$\frac{\Delta T}{T} = \frac{T_{pump-on} - T_{pump-off}}{T_{pump-off}} \quad (2)$$

GIWAXS. GIWAXS measurements were carried out with a Xeuss 2.0 SAXS/WAXS laboratory beamline using a Cu X-ray source (8.05 keV, 1.54 Å) and a Pilatus3R 300K detector. The incidence angle is 0.2°.

Supporting Figures

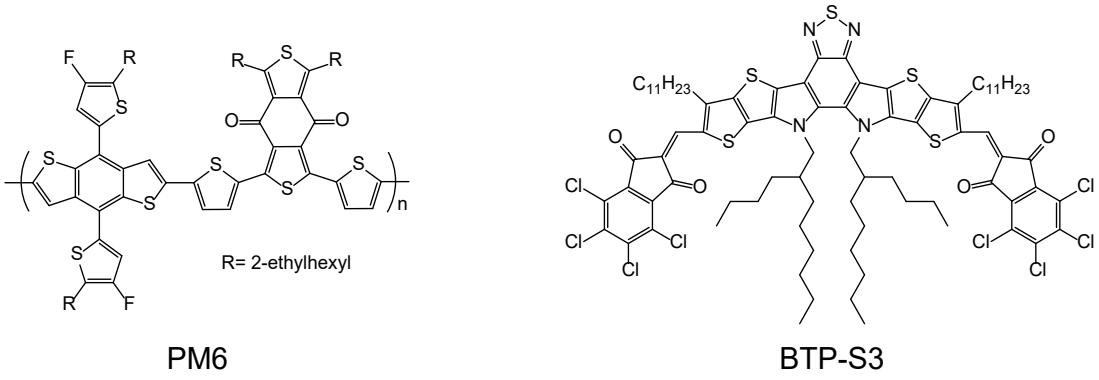

Figure S1. Chemical structures of PM6 and BTP-S3.

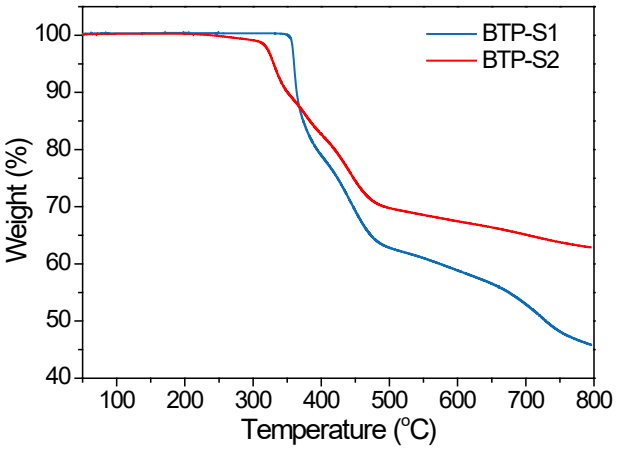

Figure S2. TGA curves of BTP-S1 and BTP-S2.

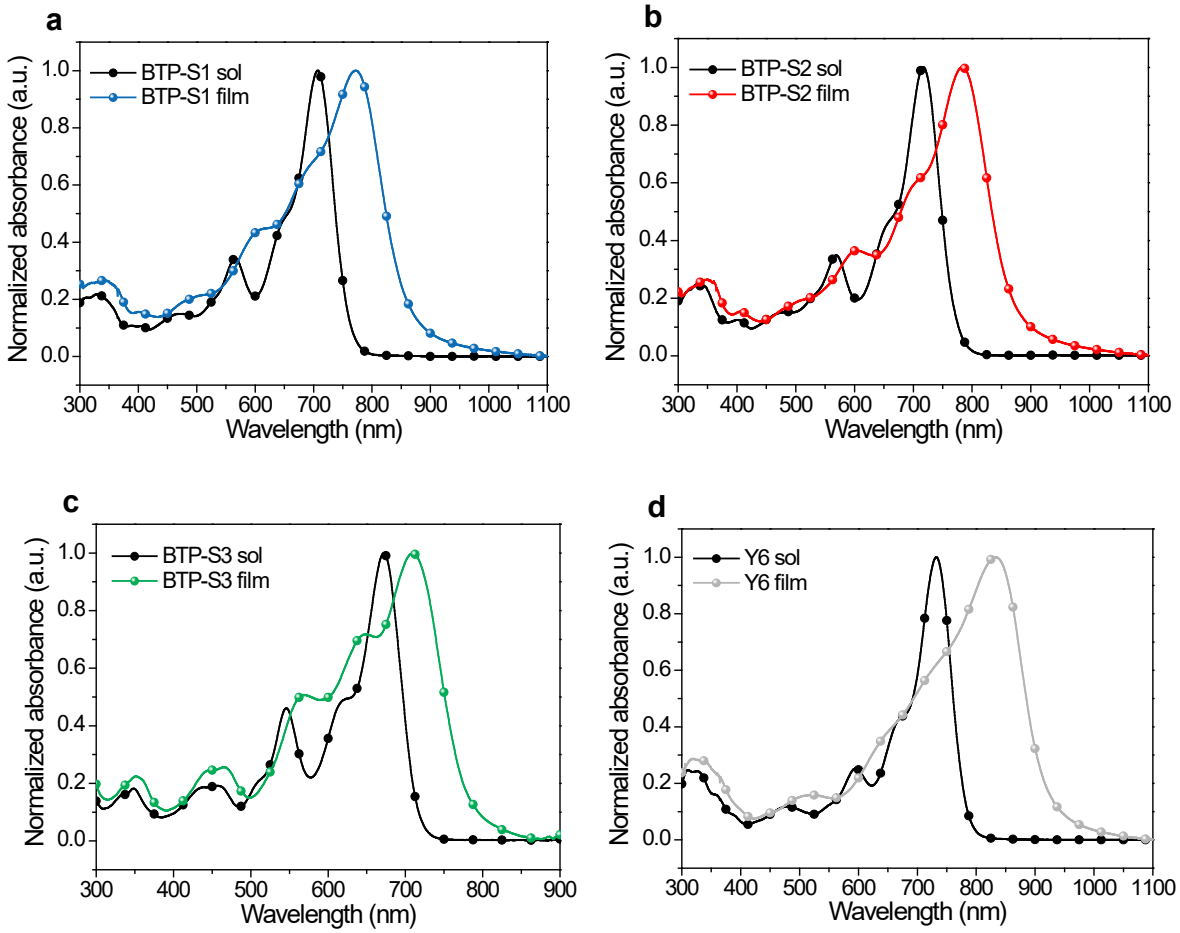

Figure S3. Normalized absorption spectra of a) BTP-S1, b) BTP-S2, c) BTP-S3 and d) Y6 in solution and film.

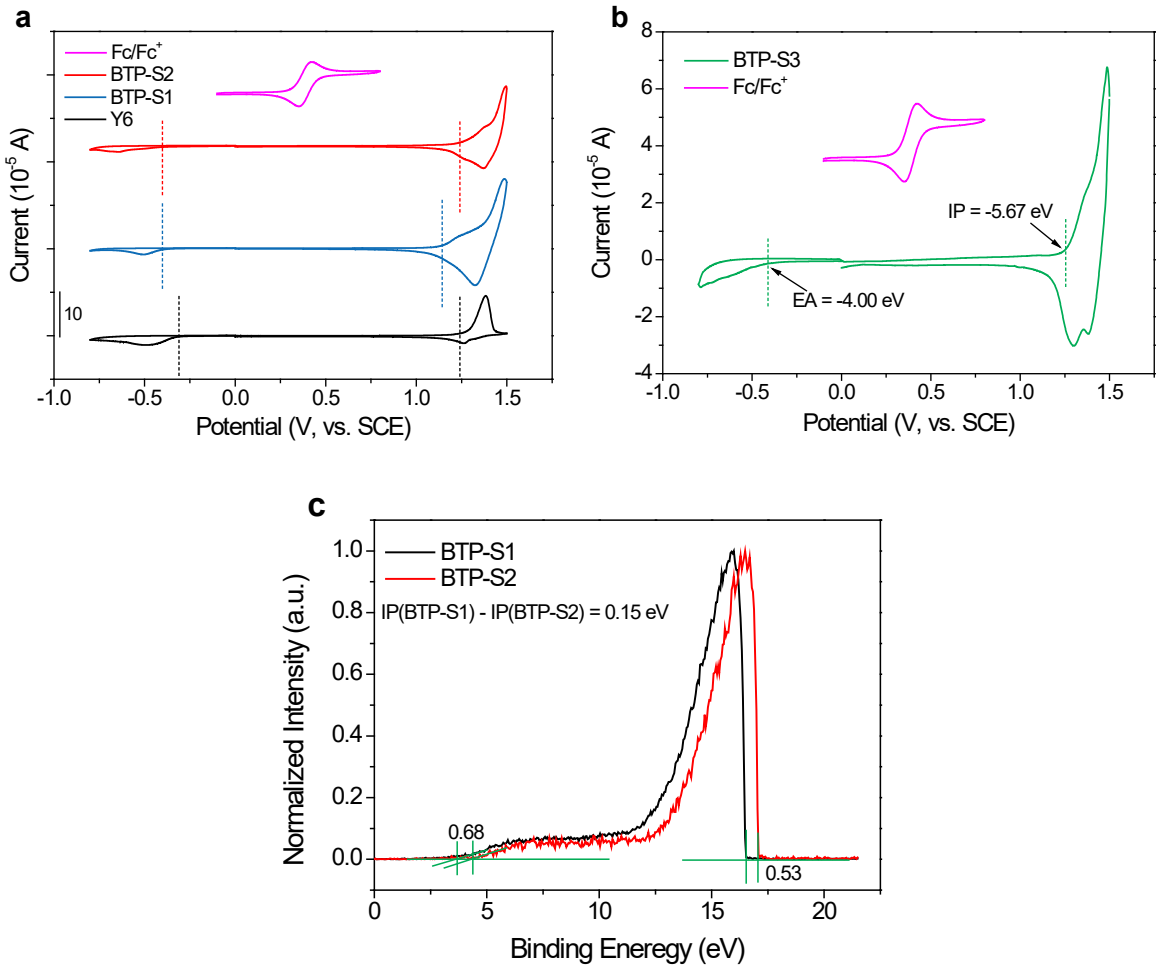

Figure S4. a) Cyclic voltammograms of BTP-S1, BTP-S2, Y6 and Fc/Fc^+. b) Cyclic voltammograms of BTP-S3 and Fc/Fc^+. c) Ultraviolet photoelectron spectroscopy (UPS) data of BTP-S1 and BTP-S2.

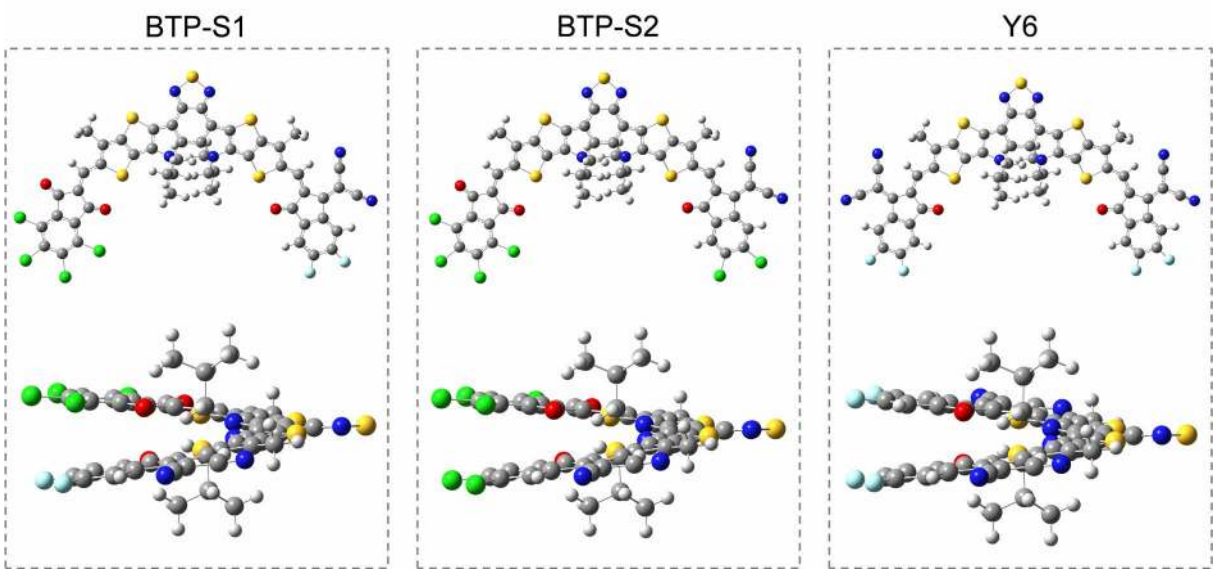

Figure S5. Geometries of BTP-S1, BTP-S2 and Y6 via density functional theory (DFT) calculations at the B3LYP/6-31G level.

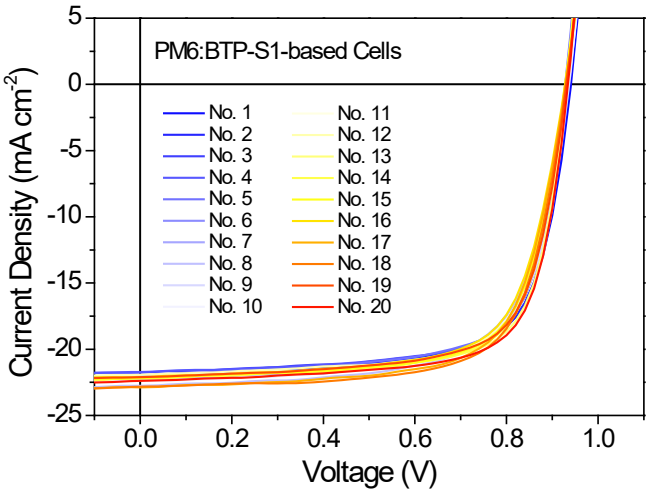

Figure S6. *J-V* curves of 20 independent OPVs based on PM6:BTP-S1 blend film.

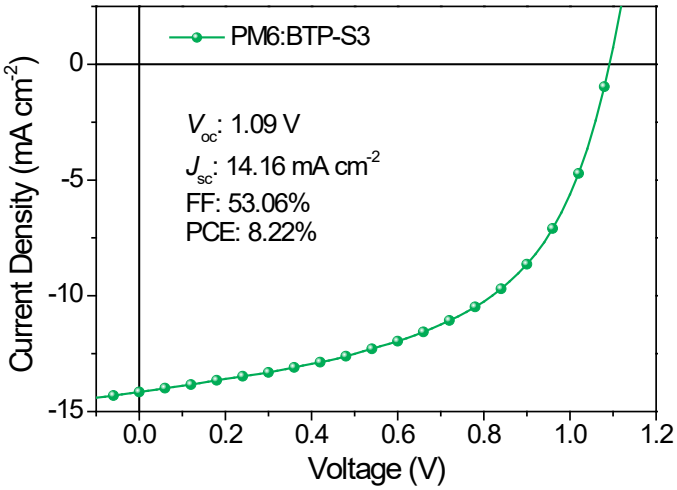

Figure S7. *J-V* curve of OPVs based on PM6:BTP-S3 blend film (Devices were fabricated under the same conditions to those of PM6:BTP-S2-based cells).

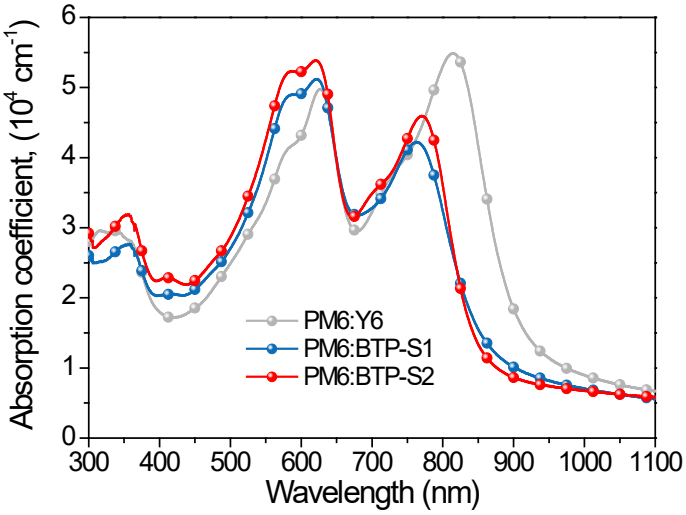

Figure S8. Absorption spectra of PM6:Y6, PM6:BTP-S1 and PM6:BTP-S2 blend films.

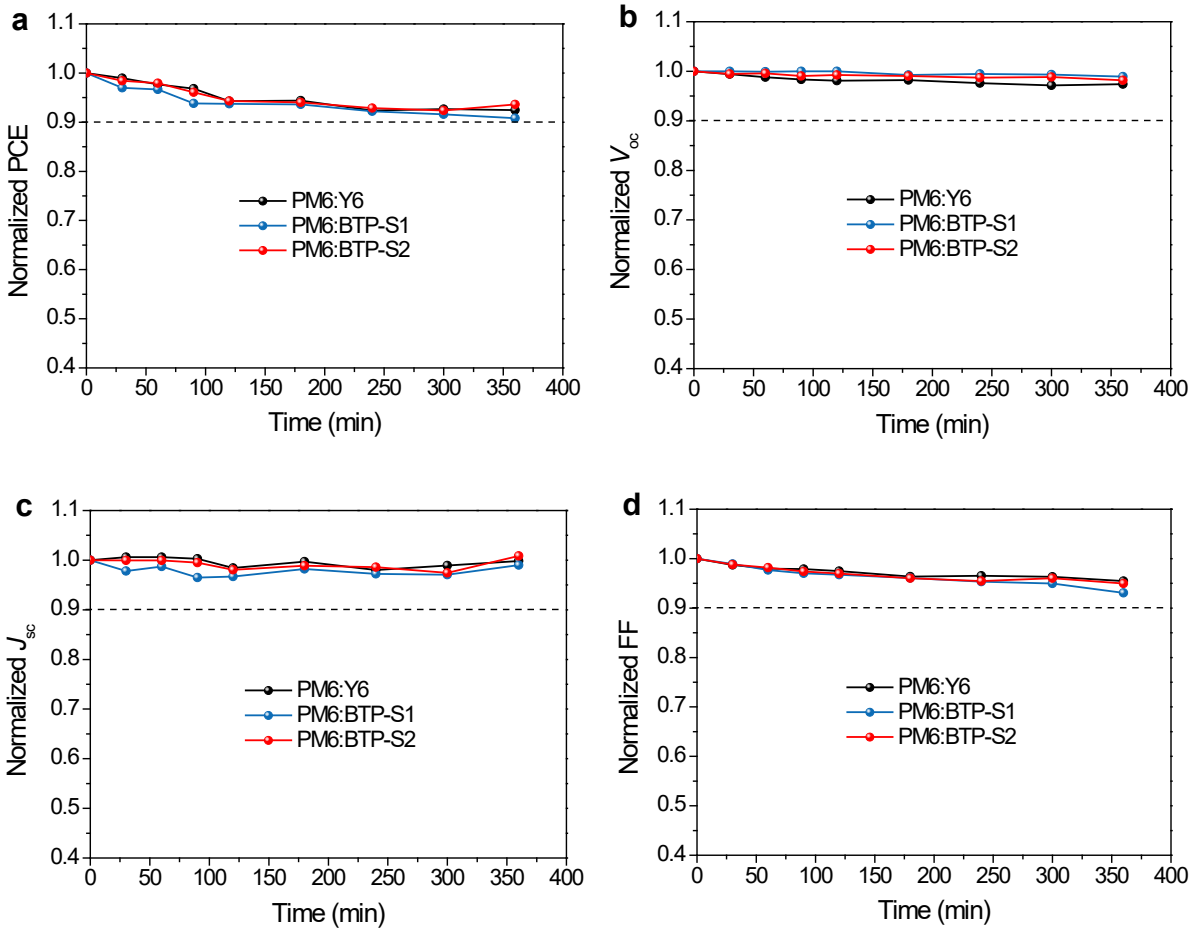

Figure S9. Time dependences of a) PCEs, b) V_{oc}s, c) J_{sc}s and d) FF for PM6:Y6-based, PM6:BTP-S1-based and PM6:BTP-S2-based cells under continuous AM 1.5G illumination at 100 mw cm^{-2} (every point is the average of four independent devices).

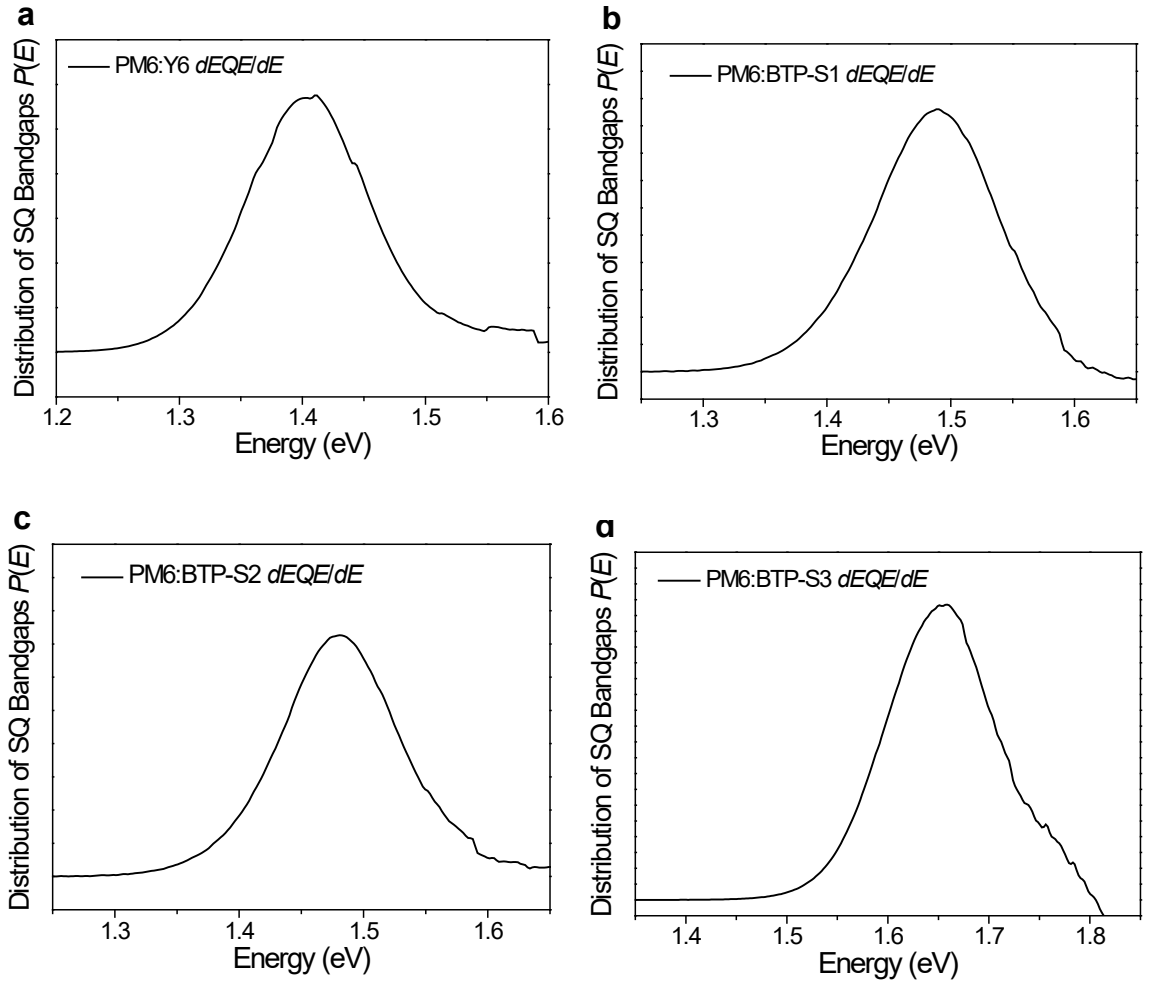

Figure S10. Distribution of SQ bandgaps P(E) for a) PM6:Y6, b) PM6:BTP-S1, c) PM6:BTP-S2 and d) PM6:BTP-S3 blends.

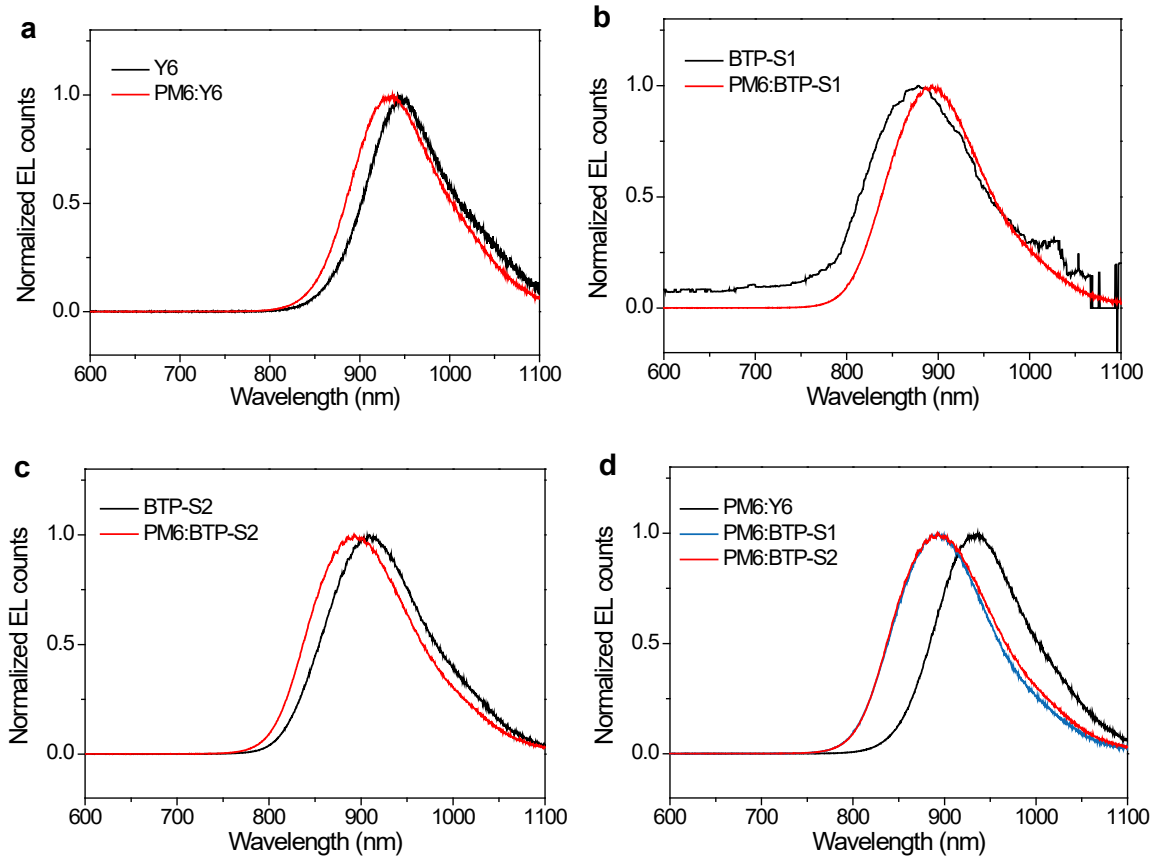

Figure S11. a) Normalized EL spectra of neat Y6 and PM6:Y6 films. b) Normalized EL spectra of neat BTP-S1 and PM6:BTP-S1 films. c) Normalized EL spectra of neat BTP-S2 and PM6:BTP-S2 films. d) Normalized EL spectra of PM6:Y6, PM6:BTP-S1 and PM6:BTP-S2 blend films.

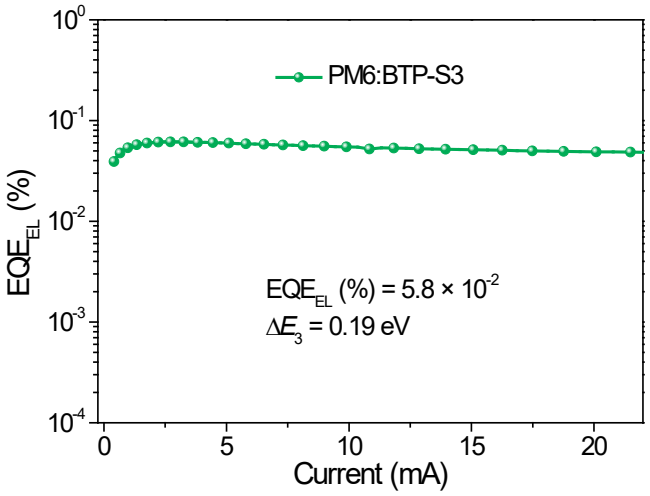

Figure S12. EL quantum efficiency of OPV based on PM6:BTP-S3 blend film.

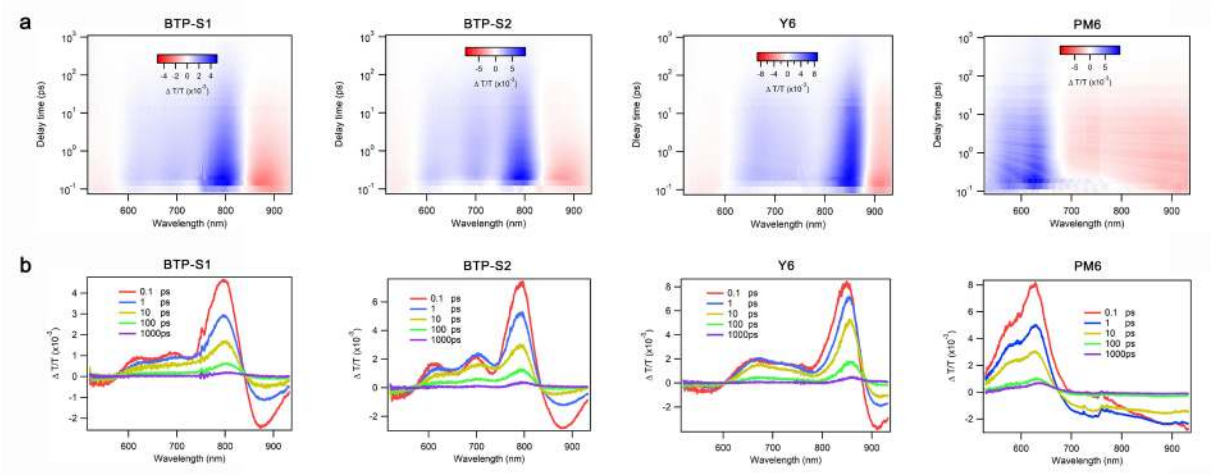

Figure S13. a) Color plot of TA spectra of neat BTP-S1, BTP-S2, Y6 and PM6 films under 750 nm excitation. b) Representative TA spectra at indicated delay time.

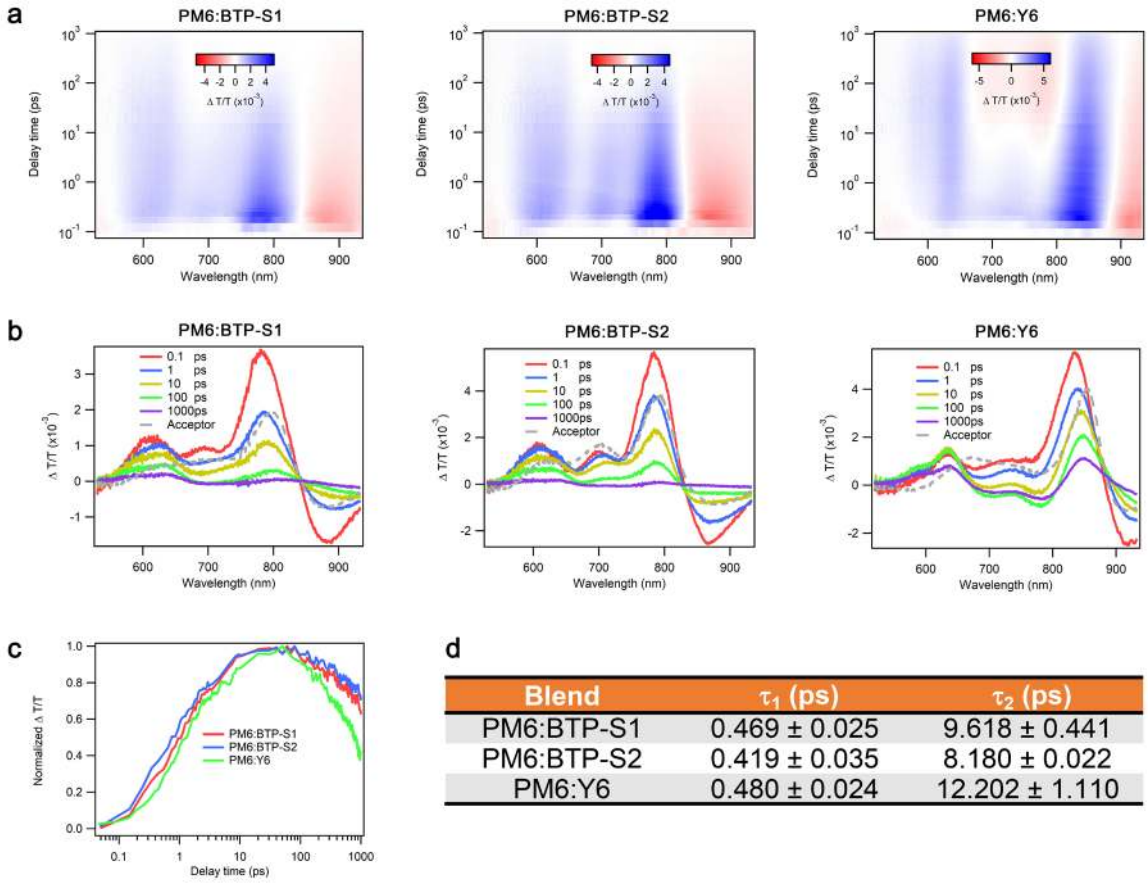

Blend	τ_1 (ps)	τ_2 (ps)
PM6:BTP-S1	0.469 ± 0.025	9.618 ± 0.441
PM6:BTP-S2	0.419 ± 0.035	8.180 ± 0.022
PM6:Y6	0.480 ± 0.024	12.202 ± 1.110

Figure S14. a) Color plot of TA spectra of PM6:BTP-S1, PM6:BTP-S2 and PM6:Y6 blends under 750 nm excitation. b) Representative TA spectra at indicated delay time (Gray dots: TA spectrum of neat acceptor films excited by 750 nm at 1 ps). c) TA kinetics of PM6:BTP-S1, PM6:BTP-S2 and PM6:Y6 blends showing the hole transfer process. d) Hole transfer time summary: τ_1 represents the exciton dissociation time at the interfaces, τ_2 represents exciton diffusion time toward interfaces before hole transfer.

Note 1 (Hole transfer process)

For hole transfer process, we applied 750 nm excitation wavelength to excite acceptors only. As shown in **Figure S13**, for neat acceptors, the bleach peaks mainly appear at 800 nm for BTP-S1 and BTP-S2 and 850 nm for Y6, conforming to the absorption of acceptors. The signals in the shorter wavelength of 550-650 or 600-700 nm will be significantly lowered with the increase of decay time. In the blends (see **Figure S14**), the main bleach peaks from the acceptors also appear, but the signal intensities in the shorter wavelength of 550-650 or 600-700 nm are still strong or even increase with the extension of decay time. These peaks at 550-650 nm match well with the absorption features of PM6, indicating the hole transfer process from the acceptor to donor. The TA kinetics of hole transfer process are thus extracted and drawn in **Figure S14c**. It's found that PM6:BTP-S2 blend shows the fastest hole transfer with time constants of τ_1 = 0.419 ± 0.035 ps and τ_2 = 8.180 ± 0.022 ps. Here, τ_1 represents the exciton dissociation time at the interfaces and τ_2 represents exciton diffusion time toward interfaces before hole transfer. We also observe that PM6:BTP-S1 blend shows faster hole transfer (τ_1 = 0.469 ± 0.025 ps, τ_2 = 9.618 ± 0.441 ps) than PM6:Y6 blend (τ_1 = 0.480 ± 0.024 ps, τ_2 = 12.202 ± 1.110 ps), though the IP offset (0.07 eV) of PM6:BTP-S1 blend is smaller than that (0.17 eV) of PM6:Y6 blend. The above results indicate that under small IP offset less than 0.2 eV, the molecular structure factor (like halogen type or number at the terminals) may make a main contribution to the hole transfer than energy level offset.

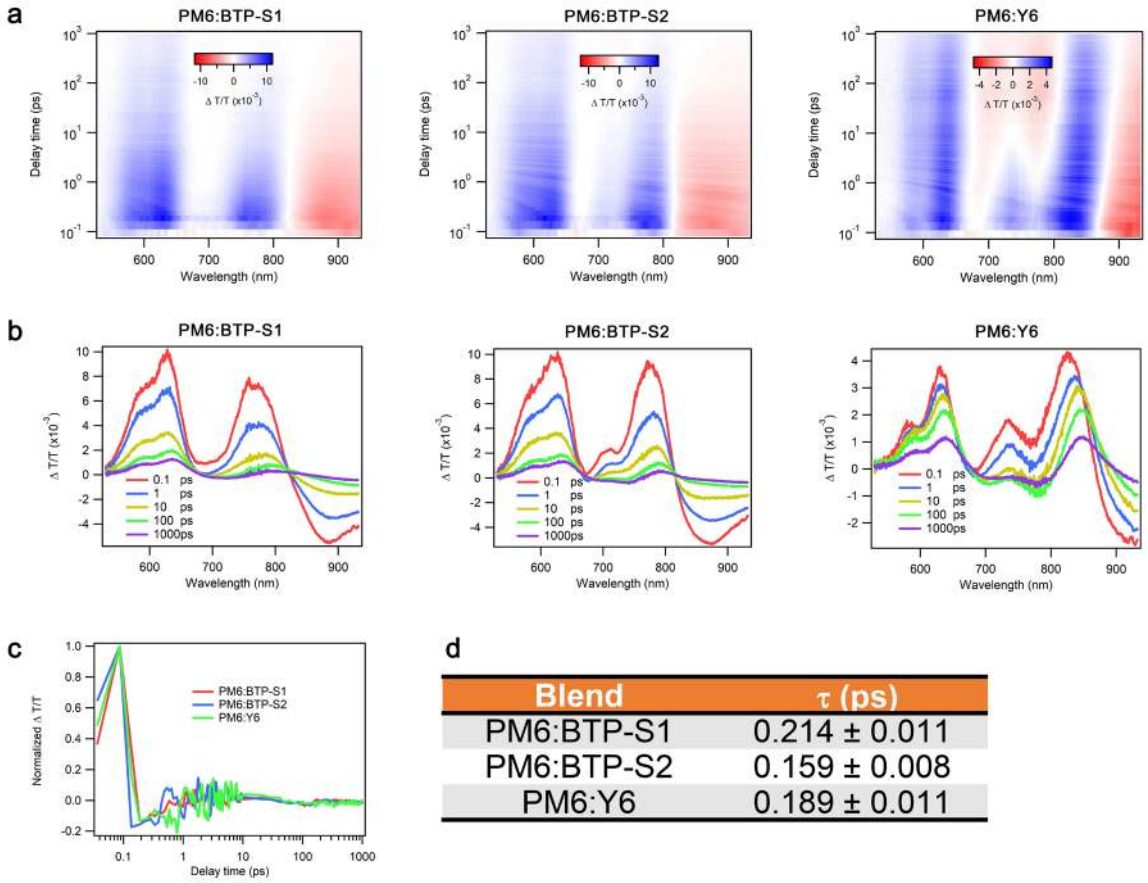

Blend	τ (ps)
PM6:BTP-S1	0.214 ± 0.011
PM6:BTP-S2	0.159 ± 0.008
PM6:Y6	0.189 ± 0.011

Figure S15. a) Color plot of TA spectra of PM6:BTP-S1, PM6:BTP-S2 and PM6:Y6 blend films under 520 nm excitation. b) Representative TA spectra at indicated delay time. c) TA kinetics of PM6:BTP-S1, PM6:BTP-S2 and PM6:Y6 blends extracted by singular value decomposition (SVD) showing the electron transfer process. d) Electron transfer time summary.

Note 2 (Electron tansfer process)

For electron transfer from the donor to acceptor, all three blends show fast electron transfer with the time constants of $\tau = 0.214 \pm 0.011$ ps for PM6:BTP-S1 blend, $\tau = 0.159 \pm 0.008$ ps for PM6:BTP-S2 blend and $\tau = 0.189 \pm 0.011$ ps for PM6:Y6 blend (**Figure S15**). In this case, more halogen atom numbers don't mean faster electron transfer. So, from the above results, we can learn that, under large EA offset more than 0.3 eV, energy level offset may be the dominant factor influencing the electron transfer speed.

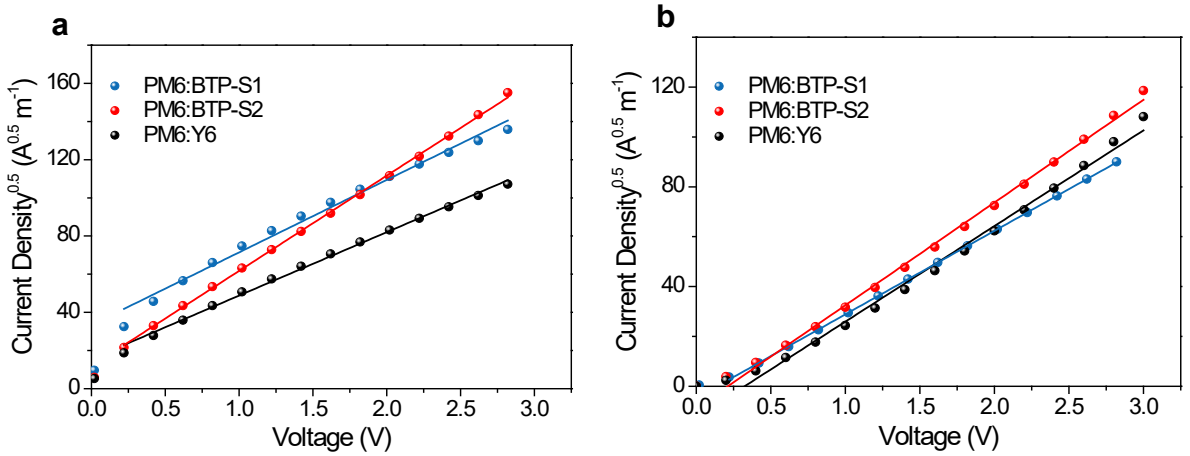

Figure S16. a) $J^{0.5}$-V curves of the hole-only devices based on PM6:BTP-S1, PM6:BTP-S2 and PM6:Y6 blend films. b) $J^{0.5}$-V curves of the electron-only devices based on PM6:BTP-S1, PM6:BTP-S2 and PM6:Y6 blend films.

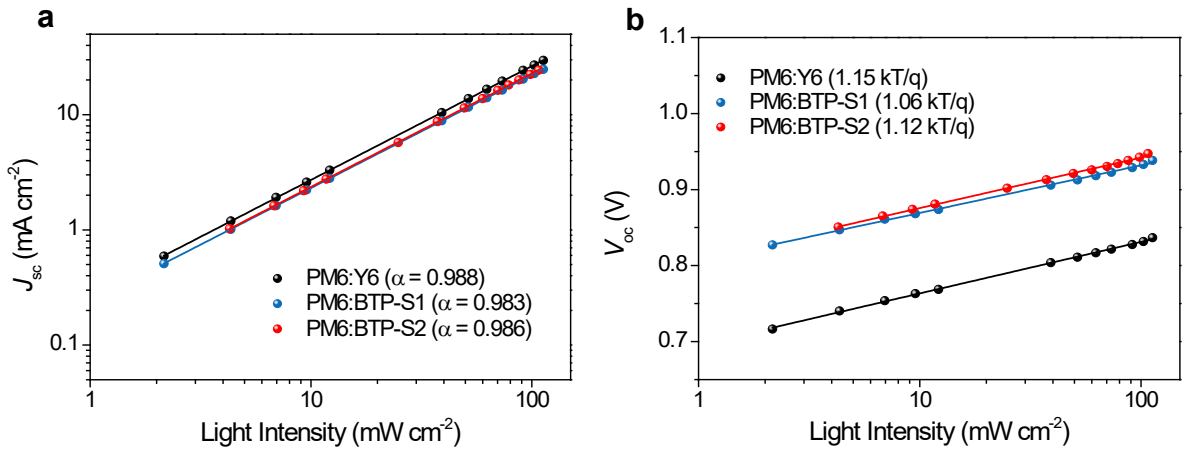

Figure S17. Dependence of a) J_{sc} and b) V_{oc} on light intensity of OPVs based on PM6:Y6, PM6:BTP-S1 and PM6:BTP-S2 blend films.

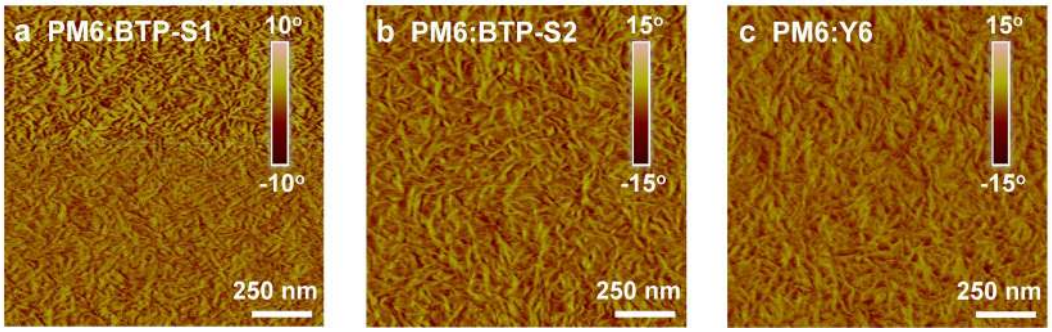

Figure S18. AFM phase images of a) PM6:BTP-S1, b) PM6:BTP-S2 and c) PM6:Y6 blend films.

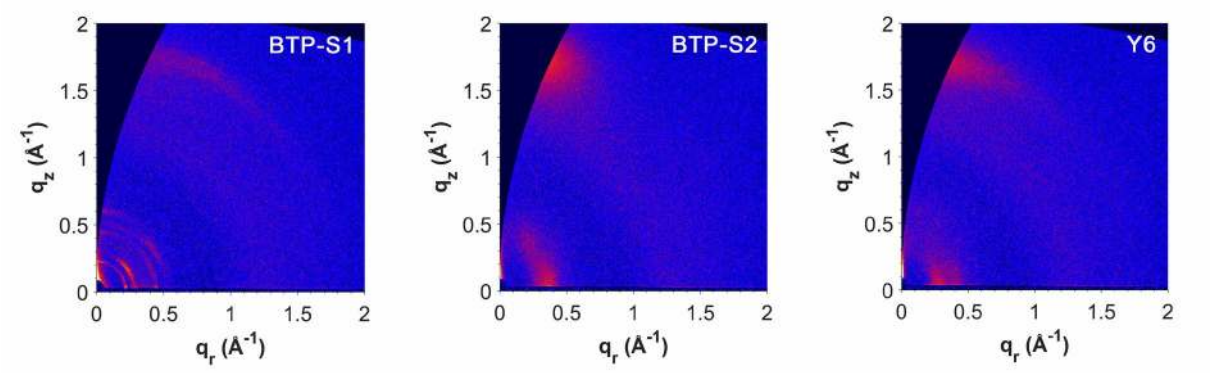

Figure S19. 2D GIWAXS images of BTP-S1, BTP-S2 and Y6 films.

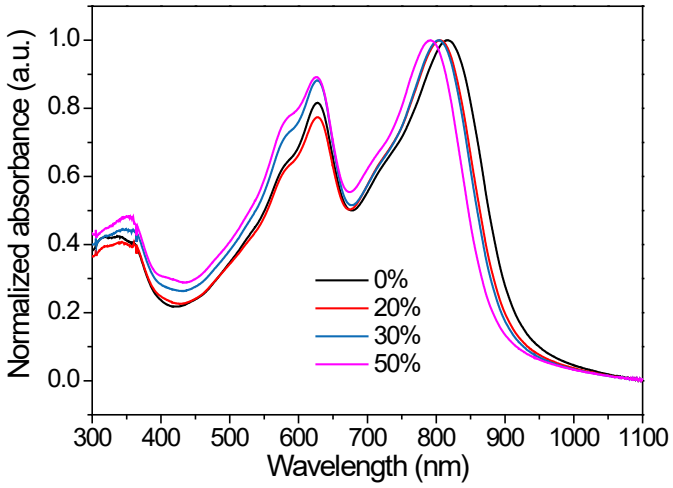

Figure S20. Absorption spectra of binary and ternary blends (0%, 20%, 30% and 50% BTP-

S2 by wt.) in thin films.

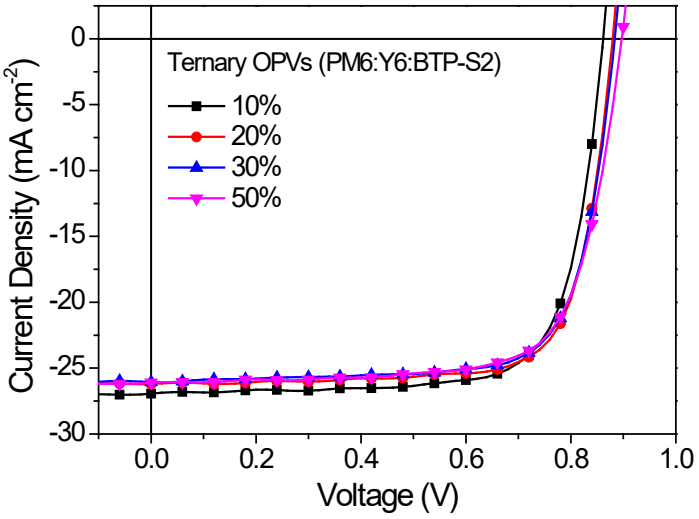

Figure S21. *J-V* curves of ternary OPVs based on PM6:Y6:BTP-S2 blend films with various BTP-S2 weight ratios in the acceptor mixture.

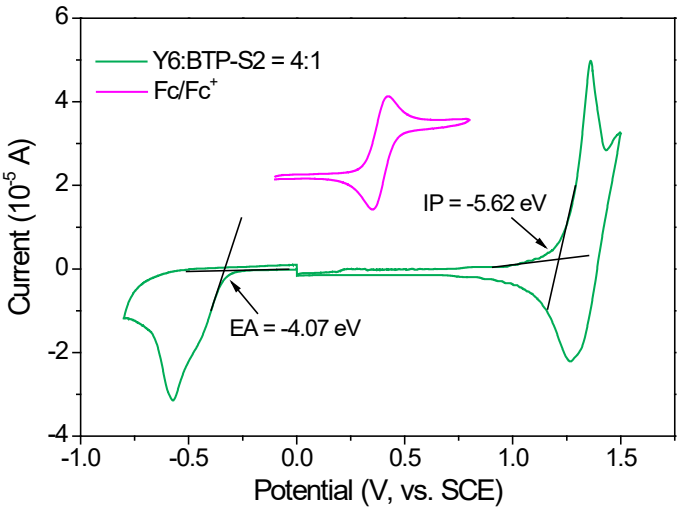

Figure S22. Cyclic voltammograms of Y6:BTP-S2 mixture (4:1, by wt.) and Fc/Fc^+.

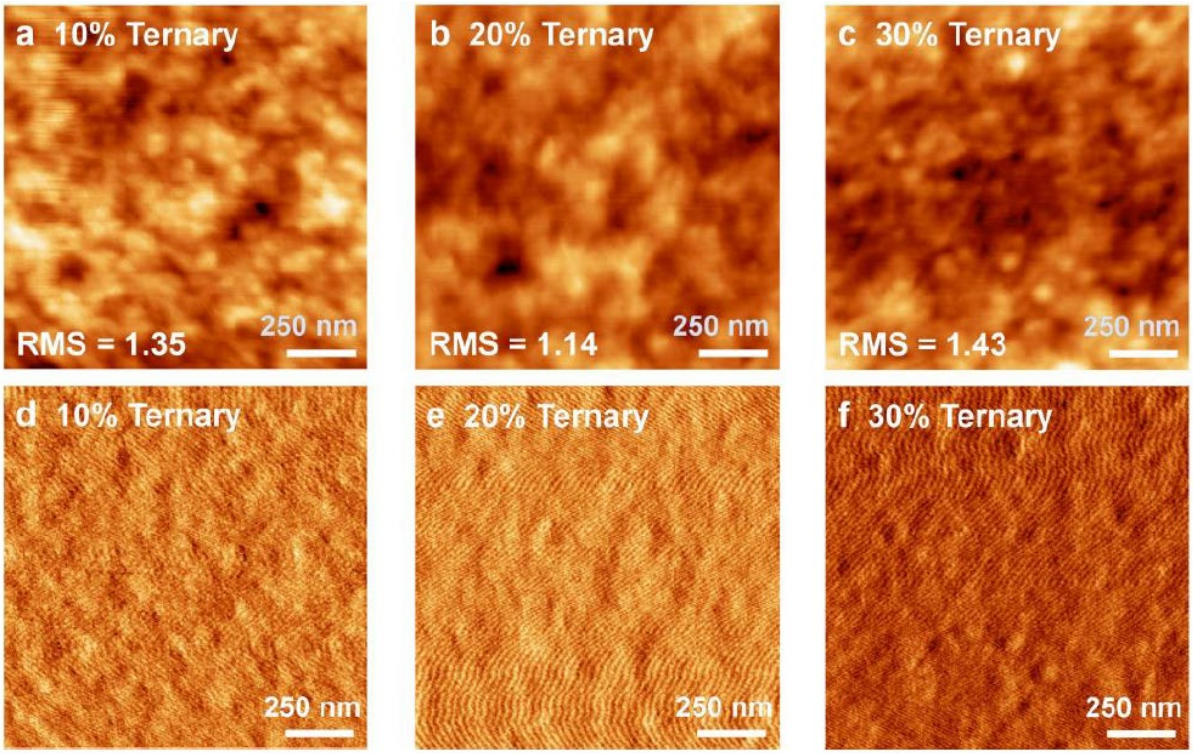

Figure S23. AFM height (a-c) and phase (d-f) images for 10%, 20% and 30% BTP-S2 by wt. Ternary blend films.

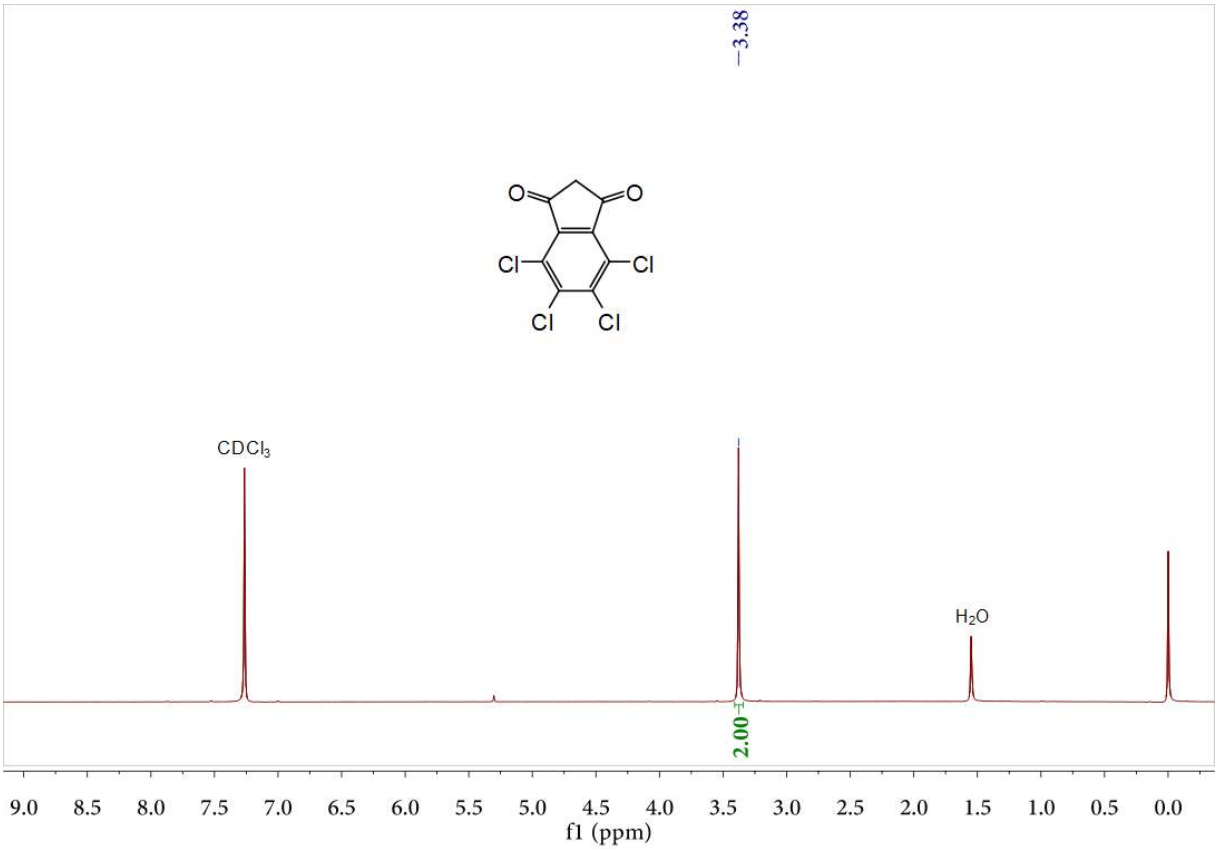

Figure S24. ^{1}H NMR spectrum of **Compound 2**.

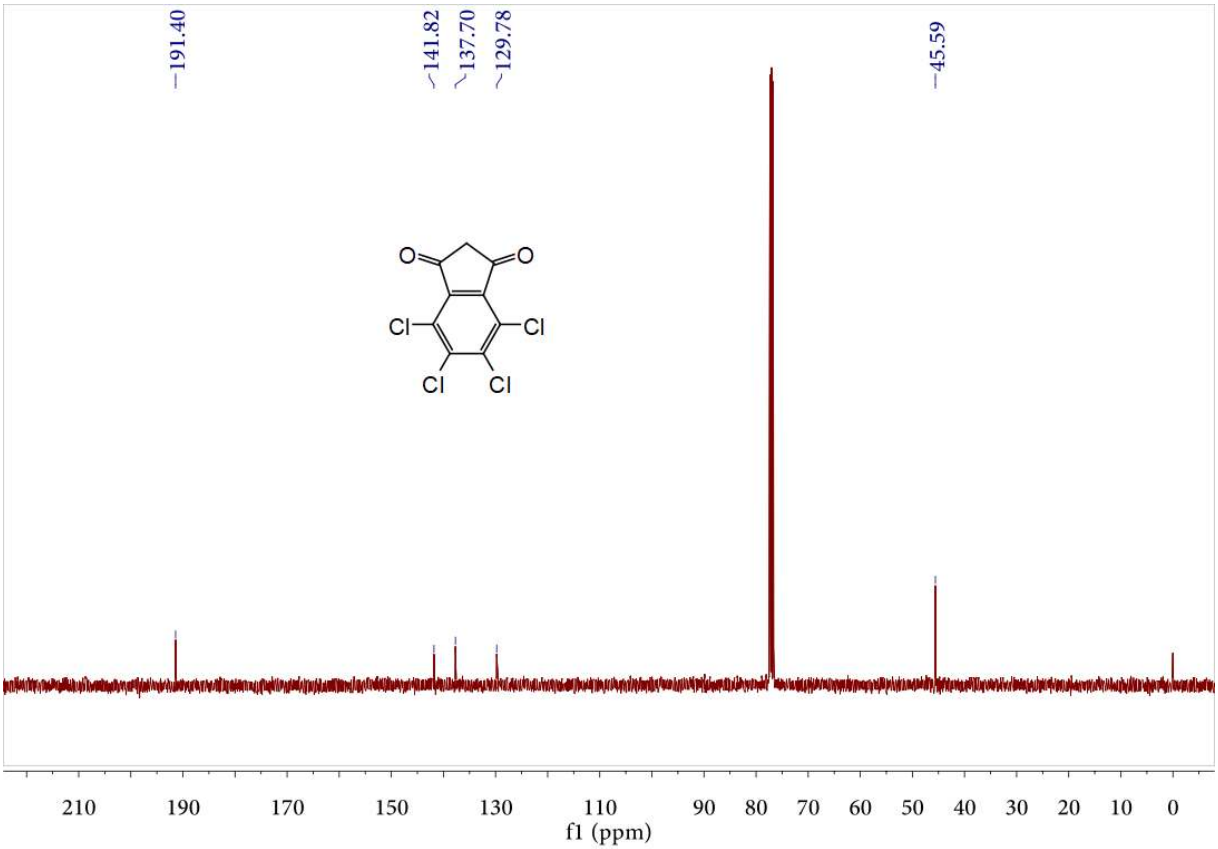

Figure S25. ^{13}C NMR spectrum of **Compound 2**.

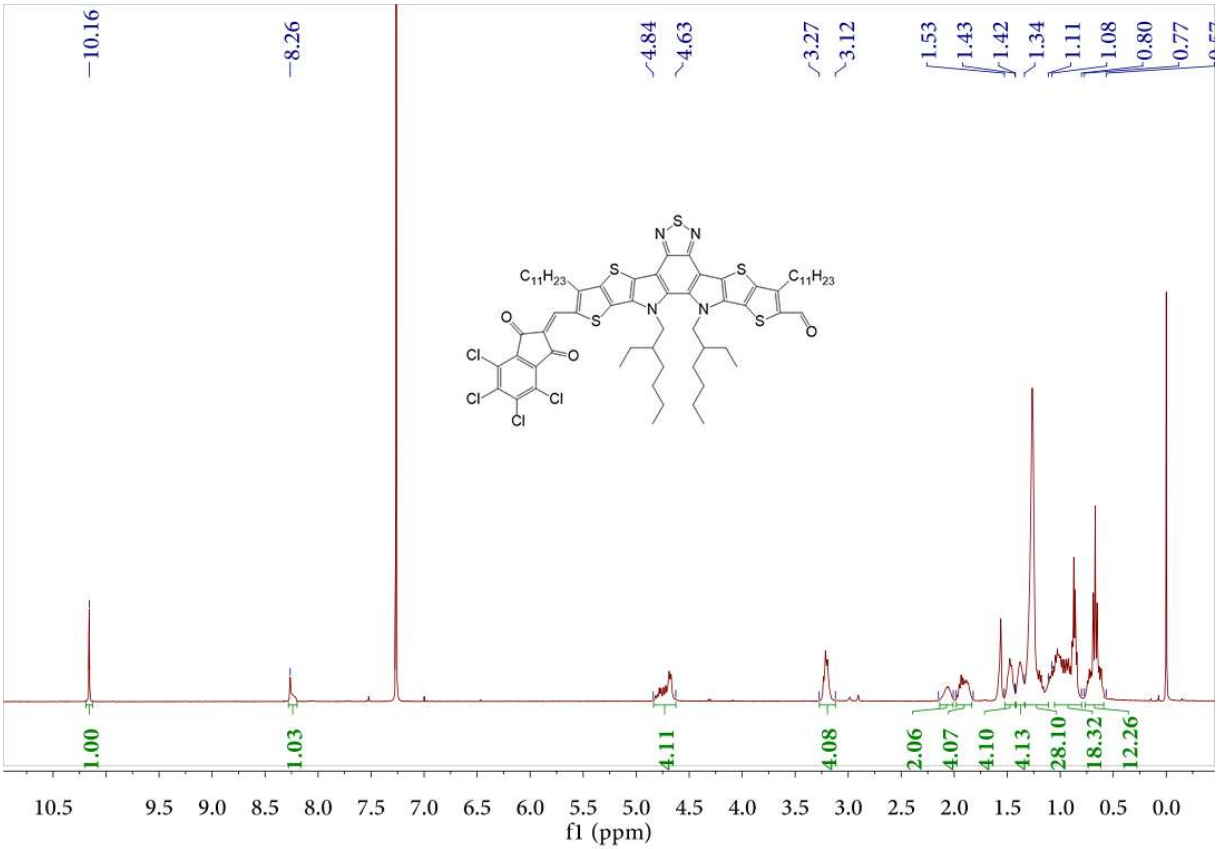

Figure S26. ^{1}H NMR spectrum of **Compound 4**.

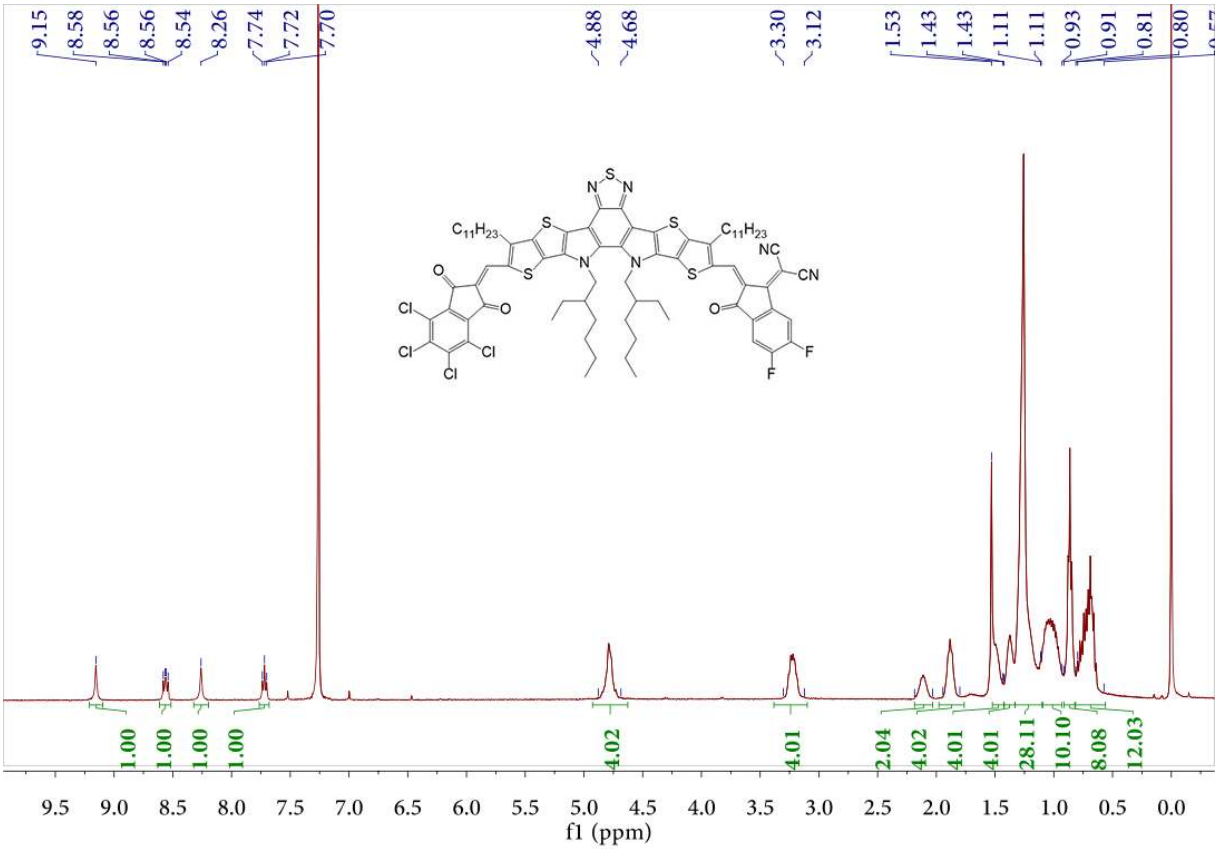

Figure S27. ^{1}H NMR spectrum of **BTP-S1**.

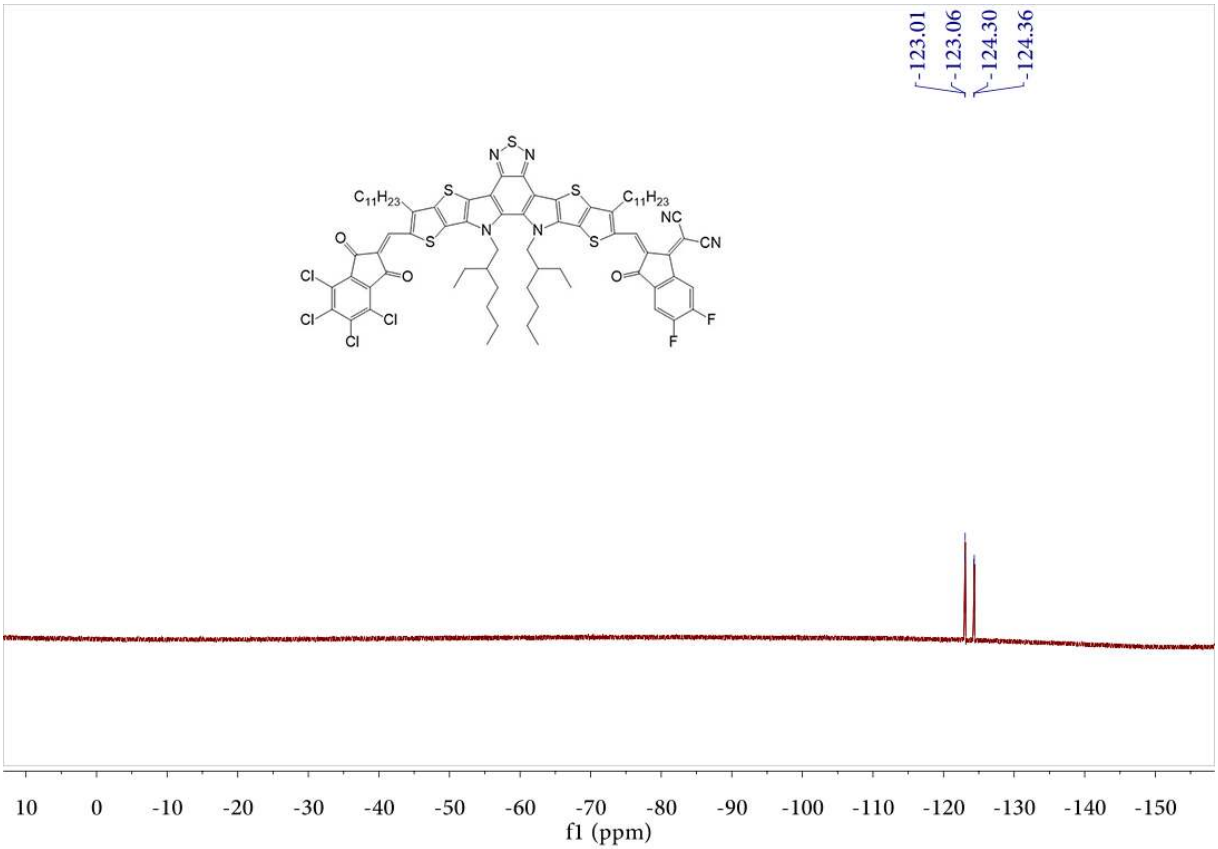

Figure S28. ^{19}F NMR spectrum of **BTP-S1**.

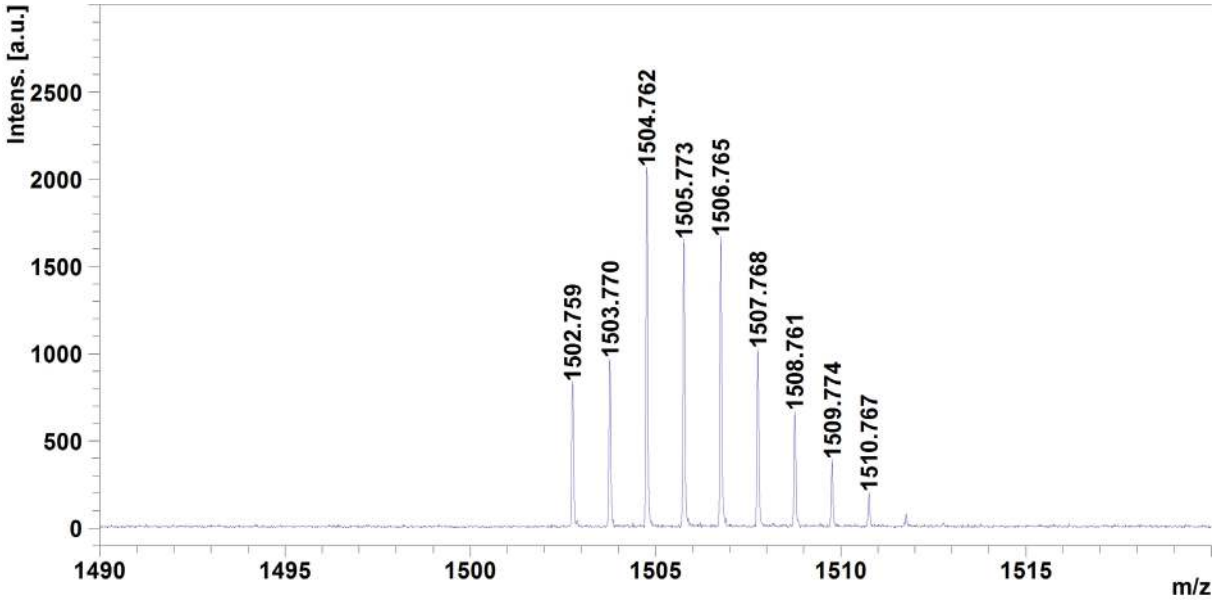

Figure S29. MALDI-TOF mass spectrum of **BTP-S1**.

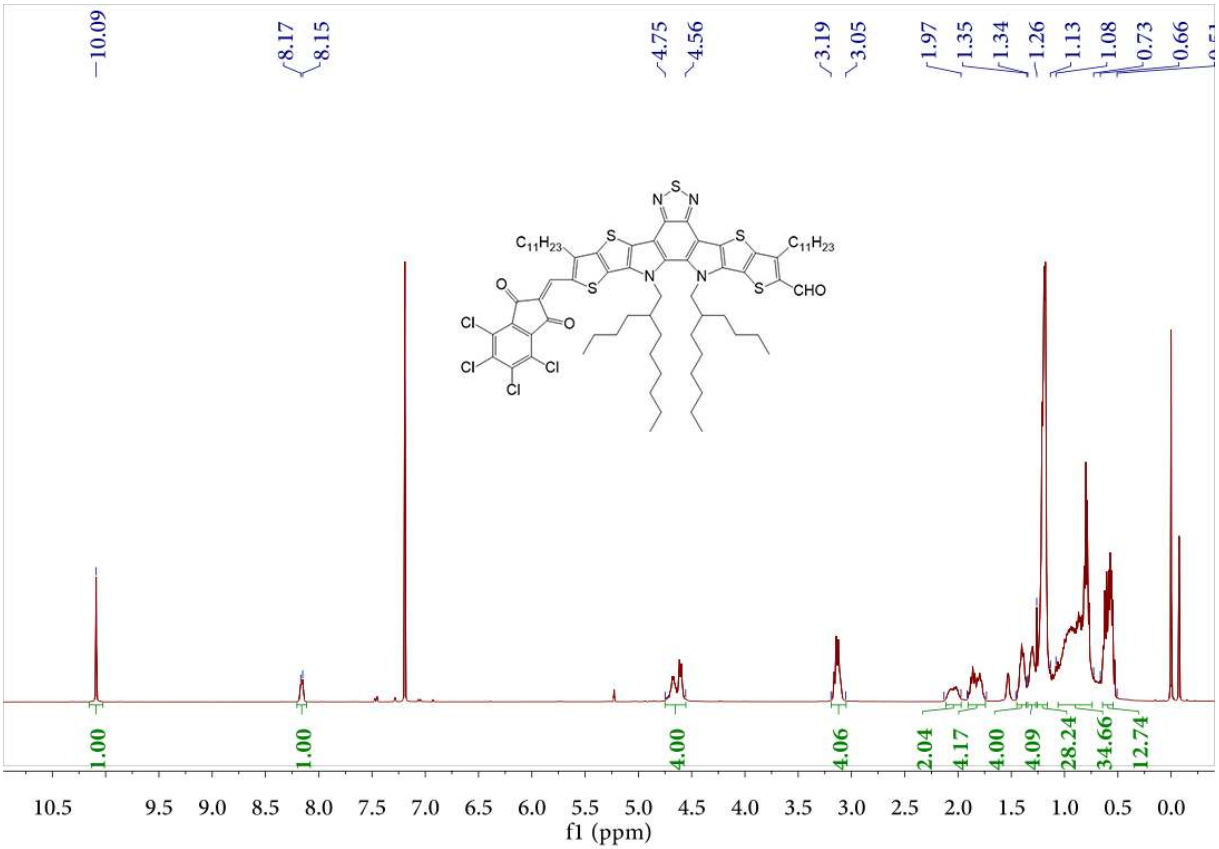

Figure S30. ^{1}H NMR spectrum of **Compound 7**.

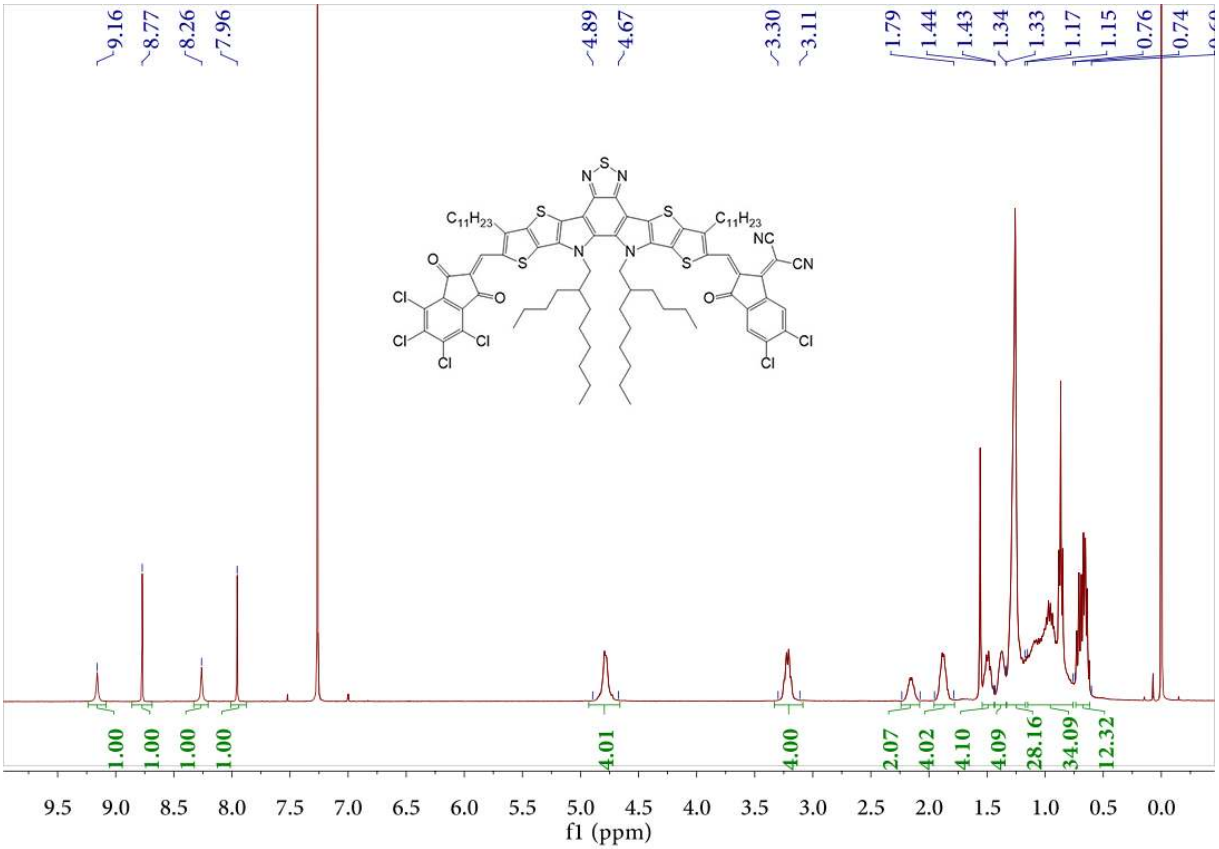

Figure S31. ^{1}H NMR spectrum of **BTP-S2**.

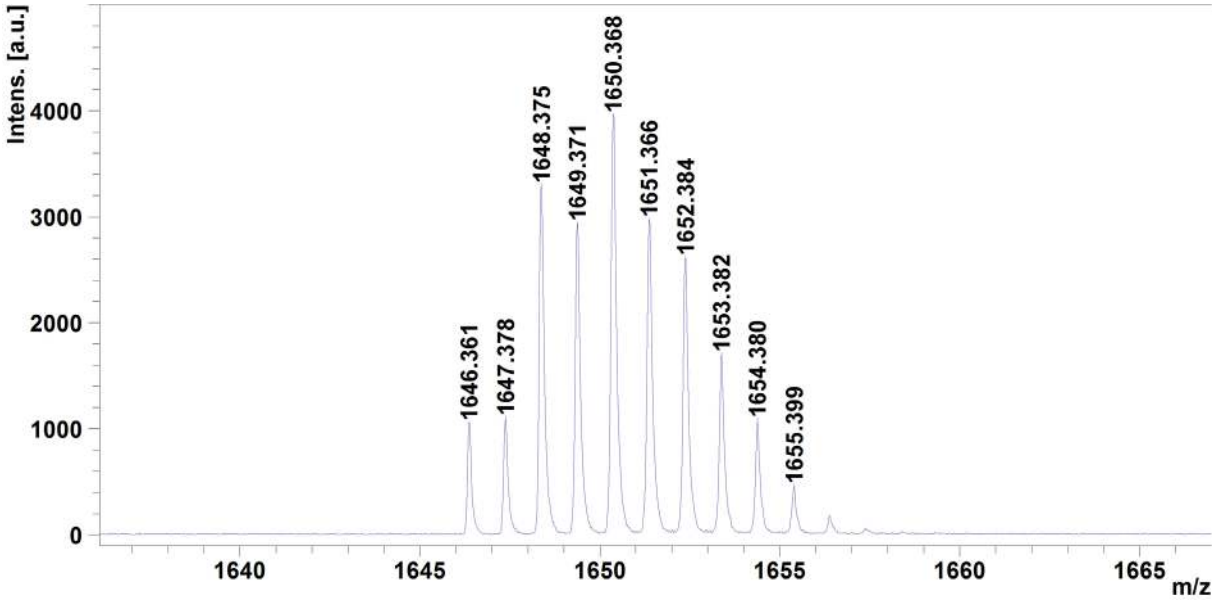

Figure S32. MALDI-TOF mass spectrum of **BTP-S2**.

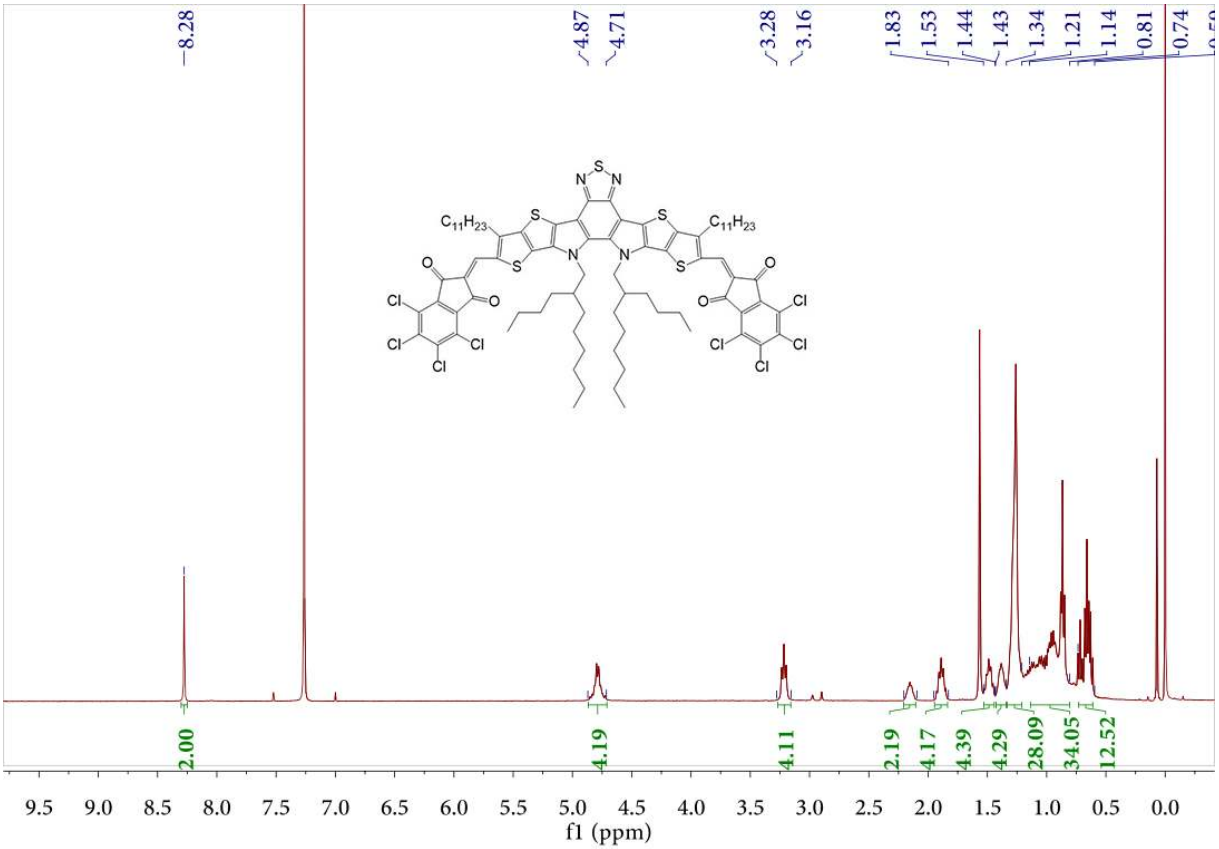

Figure S33. ^{1}H NMR spectrum of **BTP-S3**.

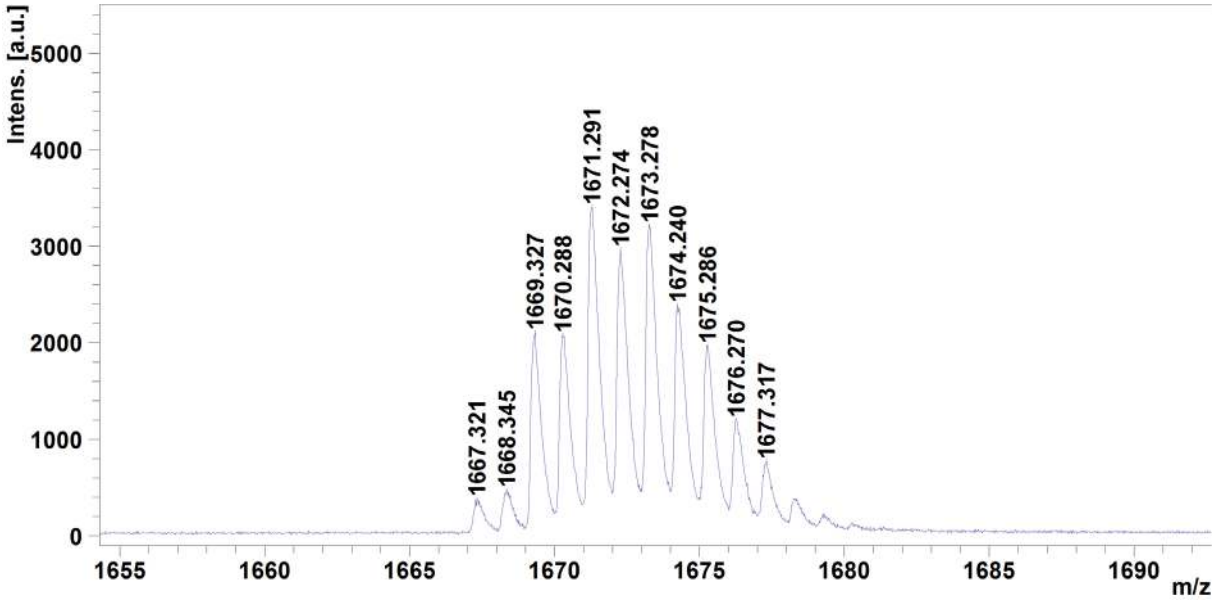

Figure S34. MALDI-TOF mass spectrum of **BTP-S3**.

Supporting Tables

Table S1. Photovoltaic parameters of OPVs based on PM6:BTP-S1 films under various optimization conditions

D:A	Annealing (°C)	CN (%)	V_{oc} (V)	J_{sc} (mA cm^{-2})	FF (%)	PCE (%)
1.2:1	w/o	w/o	0.953	17.75	55.72	9.47 (9.33 ± 0.10)
1:1	w/o	w/o	0.955	18.74	56.43	10.14 (10.02 ± 0.08)
1:1.2	w/o	w/o	0.943	18.68	57.01	10.08 (9.86 ± 0.14)
1.2:1	100	w/o	0.947	18.95	59.11	10.66 (10.54 ± 0.08)
1:1	100	w/o	0.948	19.54	59.68	11.10 (11.01 ± 0.06)
1:1.2	100	w/o	0.936	18.96	59.33	10.57 (10.48 ± 0.08)
1:1	100	0.5	0.947	20.70	68.67	13.41 (13.32 ± 0.06)
1:1	100	0.8	0.934	22.39	72.69	15.21 (14.67 ± 0.24)
1:1	100	1.0	0.920	21.00	73.21	14.09 (13.95 ± 0.15)
1:1	120	0.8	0.927	21.60	71.05	14.18 (14.13 ± 0.03)
1:1	140	0.8	0.930	21.83	71.17	14.40 (14.32 ± 0.07)

Table S2. Photovoltaic parameters of OPVs based on PM6:BTP-S2 films under various optimization conditions

D:A	Annealing (°C)	CN (%)	V_{oc} (V)	J_{sc} (mA cm^{-2})	FF (%)	PCE (%)
1:1	w/o	w/o	0.966	20.67	66.41	13.28 (13.16 ± 0.09)
1:1.2	w/o	w/o	0.961	21.42	67.95	14.01 (13.83 ± 0.23)
1:1.5	w/o	w/o	0.955	19.80	67.29	12.75 (12.64 ± 0.06)
1:1	100	w/o	0.957	21.27	69.46	14.17 (14.03 ± 0.11)
1:1.2	100	w/o	0.949	21.87	70.35	14.63 (14.54 ± 0.09)
1:1.5	100	w/o	0.938	20.25	68.72	13.08 (12.77 ± 0.41)
1:1.2	100	0.25	0.951	22.82	71.71	15.51 (15.32 ± 0.15)
1:1.2	100	0.5	0.950	22.48	73.28	15.61 (15.40 ± 0.16)
1:1.2	100	0.8	0.923	20.77	73.44	14.12 (13.95 ± 0.13)
1:1.2	115	0.5	0.945	24.07	72.02	16.37 (15.84 ± 0.21)
1:1.2	120	0.5	0.942	23.69	72.16	16.11 (15.67 ± 0.38)

Table S3. Summary of E_g, V_{oc}, E_{loss}, ΔE_{nr} and PCE of this work and reported references

Blend	E_g (eV)	V_{oc} (V)	E_{loss} (eV)	ΔE_{nr} (eV)	PCE (%)	Ref.
PM6:BTP-S1	1.49	0.93	0.56	0.22	15.21	This Work
PM6:BTP-S2	1.48	0.95	0.53	0.20	16.37	This Work
PM6:Y6:BTP-S2 (20%)	1.42	0.88	0.54	/	17.43	This Work
PM6:Y6:BTP-S2 (50%)	1.42	0.90	0.52	/	17.06	This Work
PBDB-T:Y1	1.44	0.87	0.57	0.25	13.42	[1]
PBDB-T:Y2	1.40	0.82	0.58	0.26	13.40	[1]
PM6:Y6	1.40	0.83	0.57	0.23	15.60	[2]
PM6:BTP-4Cl	1.40	0.87	0.53	0.21	16.50	[2]
PM6:BTP-4F-12	1.40	0.85	0.55	/	16.40	[3]
PM6:ITCPTC	1.65	0.95	0.70	0.36	12.30	[4]
PM6:ITC-2Cl	1.58	0.91	0.67	0.32	13.60	[4]
PM6:IT-4F	1.60	0.87	0.73	0.37	12.90	[4]
PM6:IT-4Cl	1.56	0.80	0.76	0.41	12.70	[4]
PBDB-T:IEICO-4F	1.35	0.75	0.60	0.28	6.64	[5]
P2F-Ehp:IT-2F	1.63	0.89	0.74	0.33	12.96	[6]
BTR:NITI:$PC_{71}BM$	1.49	0.94	0.55	0.30	13.63	[7]
PFBDB-T:C8-ITIC	1.53	0.93	0.60	0.33	13.20	[8]
PffBT2T-TT:O-IDTBR	1.60	1.05	0.55	0.24	10.40	[9]
S1:Y6	1.41	0.87	0.54	0.23	16.42	[10]
J71:ITC6-IC	1.67	0.95	0.72	0.37	10.41	[11]
PTQ10:Y6	1.42	0.87	0.55	0.23	16.21	[12]
L2:TTPT-T-4F	1.58	0.86	0.72	0.33	14.00	[13]
PTB7-Th:PBDTm-T1:FOIC	1.38	0.76	0.62	0.27	13.80	[14]
PBDB-T:DOC2C6-2F	1.42	0.85	0.57	0.27	13.24	[15]
PM6:Y6:3TP3T-4F	1.41	0.85	0.56	0.22	16.70	[16]
ZR1:Y6	1.40	0.86	0.54	0.24	14.34	[17]

Table S4. Summary of hole and electron mobilities of PM6:BTP-S1, PM6:BTP-S2 and PM6:Y6-based devices.

Blend	μ_h ($\times 10^{-4}$ cm^2 V^{-1} s^{-1})	μ_e ($\times 10^{-4}$ cm^2 V^{-1} s^{-1})	μ_h / μ_e
PM6:BTP-S1	5.19 ± 2.41	4.16 ± 1.28	1.25
PM6:BTP-S2	12.12 ± 4.92	8.29 ± 2.61	1.46
PM6:Y6	5.40 ± 1.90	6.57 ± 2.24	0.82

Supporting References

[1] J. Yuan, T. Huang, P. Cheng, Y. Zou, H. Zhang, J. L. Yang, S.-Y. Chang, Z. Zhang, W. Huang, R. Wang, D. Meng, F. Gao, Y. Yang, *Nat. Commun.* **2019**, *10*, 570.

[2] Y. Cui, H. Yao, J. Zhang, T. Zhang, Y. Wang, L. Hong, K. Xian, B. Xu, S. Zhang, J. Peng, Z. Wei, F. Gao, J. Hou, *Nat. Commun.* **2019**, *10*, 2515.

[3] L. Hong, H. Yao, Z. Wu, Y. Cui, T. Zhang, Y. Xu, R. Yu, Q. Liao, B. Gao, K. Xian, H. Y. Woo, Z. Ge, J. Hou, *Adv. Mater.* **2019**, *31*, 1903441.

[4] Z. Luo, T. Liu, Y. Wang, G. Zhang, R. Sun, Z. Chen, C. Zhong, J. Wu, Y. Chen, M. Zhang, Y. Zou, W. Ma, H. Yan, J. Min, Y. Li, C. Yang, *Adv. Energy Mater.* **2019**, *9*, 1900041.

[5] L. Zhan, S. Li, H. Zhang, F. Gao, T.-K. Lau, X. Lu, D. Sun, P. Wang, M. Shi, C.-Z. Li, H. Chen, *Adv. Sci.* **2018**, *5*, 1800755.

[6] B. Fan, X. Du, F. Liu, W. Zhong, L. Ying, R. Xie, X. Tang, K. An, J. Xin, N. Li, W. Ma, C. J. Brabec, F. Huang, Y. Cao, *Nat. Energy* **2018**, *3*, 1051.

[7] Z. Zhou, S. Xu, J. Song, Y. Jin, Q. Yue, Y. Qian, F. Liu, F. Zhang, X. Zhu, *Nat. Energy* **2018**, *3*, 952.

[8] Z. Fei, F. D. Eisner, X. Jiao, M. Azzouzi, J. A. Röhr, Y. Han, M. Shahid, A. S. R. Chesman, C. D. Easton, C. R. McNeill, T. D. Anthopoulos, J. Nelson, M. Heeney, *Adv. Mater.* **2018**, *30*, 1705209.

[9] S. Chen, Y. Wang, L. Zhang, J. Zhao, Y. Chen, D. Zhu, H. Yao, G. Zhang, W. Ma, R. H. Friend, P. C. Y. Chow, F. Gao, H. Yan, *Adv. Mater.* **2018**, *30*, 1804215.

[10] H. Sun, T. Liu, J. Yu, T.-K. Lau, G. Zhang, Y. Zhang, M. Su, Y. Tang, R. Ma, B. Liu, J. Liang, K. Feng, X. Lu, X. Guo, F. Gao, H. Yan, *Energy Environ. Sci.* **2019**, *12*, 3328.

[11] R. Sun, J. Guo, Q. Wu, Z. Zhang, W. Yang, J. Guo, M. Shi, Y. Zhang, S. Kahmann, L. Ye, X. Jiao, M. A. Loi, Q. Shen, H. Ade, W. Tang, C. J. Brabec, J. Min, *Energy Environ. Sci.* **2019**, *12*, 3118.

[12] C. Sun, F. Pan, S. Chen, R. Wang, R. Sun, Z. Shang, B. Qiu, J. Min, M. Lv, L. Meng, C. Zhang, M. Xiao, C. Yang, Y. Li, *Adv. Mater.* **2019**, *31*, 1905480.

[13] X. Li, K. Weng, H. S. Ryu, J. Guo, X. Zhang, T. Xia, H. Fu, D. Wei, J. Min, Y. Zhang, H. Y. Woo, Y. Sun, *Adv. Funct. Mater.* **2020**, *30*, 1906809.

[14] Y. Xie, T. Li, J. Guo, P. Bi, X. Xue, H. S. Ryu, Y. Cai, J. Min, L. Huo, X. Hao, H. Y. Woo, X. Zhan, Y. Sun, *ACS Energy Lett.* **2019**, *4*, 1196.

[15] H. Huang, Q. Guo, S. Feng, C. e. Zhang, Z. Bi, W. Xue, J. Yang, J. Song, C. Li, X. Xu, Z. Tang, W. Ma, Z. Bo, *Nat. Commun.* **2019**, *10*, 3038.

[16] J. Song, C. Li, L. Zhu, J. Guo, J. Xu, X. Zhang, K. Weng, K. Zhang, J. Min, X. Hao, Y. Zhang, F. Liu, Y. Sun, *Adv. Mater.* **2019**, *31*, 1905645.

[17] R. Zhou, Z. Jiang, C. Yang, J. Yu, J. Feng, M. A. Adil, D. Deng, W. Zou, J. Zhang, K. Lu, W. Ma, F. Gao, Z. Wei, *Nat. Commun.* **2019**, *10*, 5393.